Analysis and experiments in preparation for measurement of blood flow during PDT treatment

Master's thesis
by
Rebecca Roos

Lund Reports on Atomic Physics, LRAP-349
Lund, September 2005

Abstract

It is important to be able to monitor the blood flow in the area of interest in treatment of superficial carcinomas with photodynamic therapy (PDT). An increase in blood flow does not only affect the amount of oxygen in the treated area, but also the penetration depth of the laser light. Since PDT treatment is dependent on oxygen, an increase in blood flow in the tumour area might increase the oxygenation, which in turn will change the effectiveness of the treatment.
This thesis aims to compare two different systems for blood flow monitoring based on different techniques, Doppler Optical Coherence Tomography (DOCT) and Laser-Doppler Perfusion Imaging (LDPI), by measurements on tissue phantoms and human skin as a preparation for measurements on skin during PDT treatment.
The study showed that both DOCT and LDPI are excellent tools for monitoring flow in tissue phantoms, and that there are recemblance between the results obtained by the DOCT system and the results obtained by the LDPI system.
Also when it comes to measurements on skin the two systems provided similar information on the time dependent perfusion after stimulation, but considering the reliability and the usability of the systems tested the LDPI system is clearly to prefer, until the DOCT system is adapted to lower flows.
When that is done, the DOCT system will probably be able to provide information on the vessel structure in the skin, and maybe on the effectiveness of for example PDT treatment.

Contents

Chapter 1

Introduction

In recent years a new method for treating cancer has been developed. This method is called photodynamic therapy (PDT) and utilises laser light and photosensitizing substances to mark and destroy tumour cells. The photosensitizer and the oxygen in the cells create a chemical reaction when illuminated with light in the right wavelength region, and the singlet oxygen created is cytotoxic. It is important to be able to monitor the blood flow in the area of interest in treatment of superficial carcinomas with photodynamic therapy (PDT). An increase in blood flow does not only change the amount of oxygen in the treated area, but also the penetration depth of the laser light. Since PDT treatment consumes oxygen, an increase in blood flow in the tumour area will increase the local blood oxygenation, which in turn will make the treatment more effective. A severe decrease in blood flow, on the other hand, can also lead to cell destruction, causing tumour damage.
The aim of this thesis is to make preclinical studies in preparation for blood flow measurements during PDT treatment, and also to make a comparison between two systems for flow measurements, namely Laser Doppler Perfusion Imaging (LDPI) and Doppler Optical Coherence Tomograph (DOCT).
The comparative study is to be performed on tissue phantoms with integrated flows and it aims to determine the axial- and lateral- resolution, as well as the systems ability to resolve different flow velocities. This is to be done as a calibration and preparation for measurements on human skin, which in turn serves as a preparation for the measurements on skin during PDT treatment.
During the measurements on human skin the changes in blood flow due to stimulation of the tissue are of interest. The blood flow is measured both before and after the provocation on the skin to determine the time dependence. The provocation is designed to affect the blood flow in the tissue volume so that it can be verified whether the sytems can detect a change in blood flow or not.
For planning of light and photosensitizer doses, knowledge of the blood perfusion and tissue oxygenation during PDT treatment is of great importance, but also knowledge of the penetration depth of the laser light when treating deeper lesions.
Hopefully, by making these comparisons, the PDT treatment can be made more effective with respect to light and photosensitizer doses.

Chapter 2

Background

2.1 Introduction to tissue optics

Light interacting with tissue can be absorbed, scattered, reflected and transmitted depending on the structure and geometry of the tissue, and its constituents. These processes are strongly wavelength dependent, and can thus be used for tissue characterization.
Light propagating in tissue will interact with the tissue through all the above mentioned processes, and hence the path of the light will be affected.
Knowledge of the interaction between light and scattering media is of great importance, since lasers have many applications, in medicine as well as in various other fields.
In the dosimetry of various medical applications information on the absorption and scattering is important when considering light doses. Depending on how the light travels and is absorbed overheating, hyperthermia, can occur resulting in tissue damage. It is also important to know how deep the light penetrates when treating tumours.
There are a few different methods for calculating the light transport through tissue and the most common theory, the transport theory, will be described in this section.

2.1.1 Light interaction with tissue

Light propagating in tissue will be absorbed and scattered due to the internal structure of the tissue. These interaction processes are strongly wavelength dependent and can therefore be used for analyzing the tissue structure, and in that way yield information on its main constituents.
The main absorbers, chromophores, in tissue in the visible, UV and NIR wavelength region are; water, lipids, melanin and haemoglobin (oxygensaturated and non-oxygensaturated), and they all have their absorbtion peaks at different wavelengths, making it possible to measure the relative amount of these absorbers by using different wavelengths. Light in the UV region is strongly absorbed due to the amount of melanin and other chromophores with absorption peaks in that region, and above 900 nm water is the main absorber with a peak around 970 nm. In the wavelength region 700-1300 nm the blood absorption decreases, making deeper penetration into tissue possible, and for that reason

this region is called the optical window, see figure 2.1.

The absorption coefficient, μ_a $[m^{-1}]$, gives the probability per unit length for a photon to be absorbed in the medium and thus it determines the inverse mean free path length in the medium. The light absorption mainly depends on the distribution and concentration of the different chromophores within the tissue [1].
When light is absorbed in tissue, molecules get excited by the absorbed energy, and that energy can be released again as heat when the molecules relax to a lower state or the molecules can send out the energy as fluorescense when decaying to the initial state.
The dominating interaction between light and tissue in the optical window is elastic scattering as a result of the inhomogenities in the refractive index in the media, caused by for example cell membrames and other scattering kernels. The scattering coefficient, μ_s $[m^{-1}]$, gives the probability per unit lenght for a photon to be scattered in the medium and thus it determines the inverse mean free path length in the medium [1].

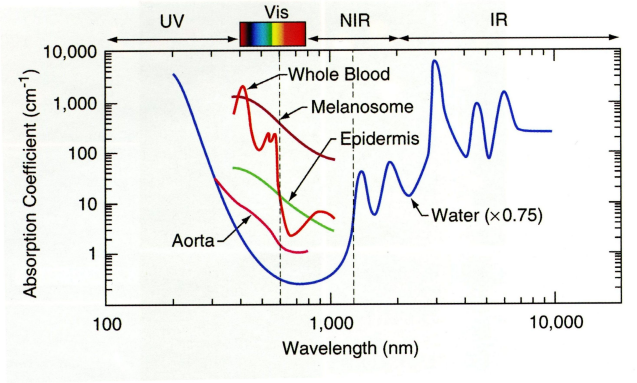

Figure 2.1: This figure shows the optical window in tissue, and the absorption curves of the main constituents [2].

When light travels through tissue it will be attenuated according to Beer-Lambert's law [3], and the attenuation coefficient, μ_t is given by equation (2.1) [1].

$$\mu_t = \mu_a + \mu_s \tag{2.1}$$

The ratio between the scattering coefficient and the total attenuation coefficient is called the albedo, a, and is given by equation (2.2) [4].

$$a = \frac{\mu_s}{\mu_a + \mu_s} \tag{2.2}$$

When photons are scattered in tissue they change direction, and the scattering phase-function is a distribution stating the probability of a photon being scattered in a specific direction.
The Henyey-Greenstein phase-function (2.3) [5], originally used for describing the scattering of light in space by interstellar dust, is a phase-function often used

to describe the scattering angle distribution for photons in biological tissue.

$$p(\Omega' \cdot \Omega) = p(\cos\theta) = \frac{1}{4\pi} \frac{1-g^2}{(1+g^2-2g\cos\theta)^{3/2}} \tag{2.3}$$

where $p(\Omega' \cdot \Omega)$ is the probability for a photon, incoming in direction Ω', to be scattered in the Ω direction, and θ is the deflection angle. Since there are several scattering events before absorption in tissue, the phase-function can be replaced by a parameter called the anisotropy factor, g, (2.4) [6].

$$g = <\cos\theta> = \int_{4\pi} \cos\theta \cdot p(\cos\theta) d\Omega \tag{2.4}$$

Forward, backward and isotropic scattering is represented by $g = 1$, $g = -1$ and $g = 0$ respectively. The effect of the anisotropy factor is illustrated in figure 2.2. In order to describe the effective scattering in tissue, the reduced scattering

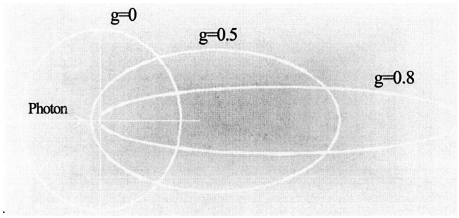

Figure 2.2: This figure illustrates how the anisotropy factor affects the propagation of light in scattering media. Different anisotropy factors, g values, result in different propagation [7].

coefficient, μ_s', can be used [8] and it is given by equation (2.5).

$$\mu_s' = (1-g)\mu_s \tag{2.5}$$

Since tissue is highly scattering, the path of the light propagating in the tissue will be affected, which is illustrated in figure 2.3.

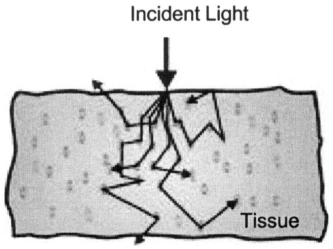

Figure 2.3: This figure illustrates the path of light in highly scattering media, such as biological tissue. The mean free path length in the tissue, i.e. the distance between absorption and scattering events, depends on the scattering- and absorption coefficients [7].

2.1.2 Light propagation in tissue

When modelling light propagation in tissue there are two main teories; wave theory and transport theory. The wave theory is based on Maxwell's equation, and the optical properties are defined by the complex dielectric constant, $\epsilon(\mathbf{r})$. The wave theory can be solved numerically, but the complex variation of $\epsilon(\mathbf{r})$ makes it difficult. Therefore mostly light propagating in very small volumes can be solved with those techniques.
The transport theory considers the light as a stream of energetic particles, photons, which are modelled by energy conservation. The medium is also considered to be homogenous containing randomly distributed absorbers and scatterers. The transport equation can be solved analytically under certain assumptions or numerically.
A third theory that can be used when dealing with spherical scatterers is Mie theory and it can be used to investigate the scattering events.

Mie theory Light scattered by spherical particles can be modeled by Mie theory. If the refractive index of the scatterers, n_p, and the media surrounding the scatterers, n_{med}, are known and the size of the scatterers is also known, then Mie calculations can give the efficiency of scattering. This theory was first presented by Gustav Mie in 1908 [9].
The efficiency of scattering relates to the cross-sectional area of scattering according to equation (2.6)

$$\sigma_s = Q_s A \tag{2.6}$$

where $A = \pi a^2$ $[cm^2]$ is the geometrical cross sectional area of the particle, Q_s is the scattering efficiency and σ_s $[cm^2]$ is the cross sectional area of scattering. The scattering coefficient, μ_s, is related to the expression in equation (2.6) according to equation (2.7)

$$\mu_s = \rho_s \sigma_s \tag{2.7}$$

where ρ_s is the scatterer number density, which is given by the ratio of the refractive index for the scatterers and the surrounding media, according to equation (2.8), and the amount of scatterers per unit volume

$$n_r = \frac{n_p}{n_{med}} \tag{2.8}$$

The transport theory Propagation of light in tissue is not easy to model, so to get an expression that could be solved either analytically or numerically, the conservation of energy in a small volume of tissue is the starting point.
The power of the propagating photons is described by the radiance, $L(r, s, t)$ $[W/m^2 sr]$, which is defined as the radiant power per unit solid angle about the unit vector s and per unit area perpendicular to s. The power, $dP(r, s, t)$ [W], that flows through a small area dA, at r, in the direction of s within the angle w, is related to the radiance according to equation (2.9) [10].

$$dP(r, s, t) = L(r, s, t) dA \cos\theta dw \tag{2.9}$$

Since photons can be absorbed irrespectively of their direction of propagation, the radiance is often replaced by the fluence rate, $\Phi(r)$ $[W/m^2]$, defined as the

radiant power incident on a small sphere, divided by the cross sectional area of that sphere, according to equation (2.10) [10].

$$\Phi(r,t) = \int_{4\pi} L(r,s,t)dw = ch\nu \int_{4\pi} N(r,s,t)dw \tag{2.10}$$

The number of photons, $N(r,s,t)$, in the volume dr^3 with direction s within dw at time t, is related to the radiance according to equation (2.10) [7].
This can be used to formulate the transport equation.
The time-resolved transport equation, (2.11), is a mathematical expression of the build-up of the photon density function N(r,s,t).
Thus the first term expresses changes in the photon distribution function with time, and the second term accounts for photon loss through the boundary. The third therm expresses the photons scattered from direction s to any other direction s', and the fourth term expresses the photons absorbed. The fifth term expresses the photons gained through scattering from any direction s' into the direction s, while the sixth term expresses the photons gained through a light source, q [7].

$$\begin{gathered}\int_V \frac{\delta N(r,s,t)}{\delta t}\delta V - \oint_S cN(r,s,t)sd\mathbf{S} - \\ \int_V c\mu_s(r)N(r,s,t)dV - \int_V c\mu_a(r)N(r,s,t)dV + \\ \int_V c\mu_s(r)\int_{4\pi} p(s',s)N(r,s',t)ds'dV + \int_V q(r,s,t)dV\end{gathered} \tag{2.11}$$

This type of equation, (2.11), can be used to model not only light in tissue, but also heat transport and flows, but since it can only be solved for the simplest cases the diffusion equation, (2.12), is used instead. The diffusion equation can be solved analytically for simple geometries, and it is derived by first expanding the photon distribution function and then mathematically simplify the equation.

$$\frac{1}{\nu}\frac{\delta}{\delta t}\rho - \nabla D\nabla\rho + \mu_a\rho = \frac{1}{\nu}q_0 \tag{2.12}$$

where: $\rho = \rho(\mathbf{r},t)$ is the photon density at position $\mathbf{r}$ at time t,
$\nu = \frac{c}{n}$ is the speed of light in the medium,
$D = \frac{1}{3\mu_t r} = \frac{1}{3(\mu_a+(1-g)\mu_s)}$ is the diffusion coefficient
q_0 is a source.

This equation, (2.12), is only valid if the reduced scattering coefficient is much larger than the absorption coefficient, $\mu_s' >> \mu_a$ [7].

The inverse problem Both the transport theory and Monte Carlo simulations can be used for solving forward problems, i.e. when the absorption- and scattering coefficients, as well as the anisotropy factor, are known. But sometimes there are needs for investigating materials with unknown optical properties, and that is called to solve an inverse problem. When both the absorption and scattering coefficients are unknown the problem is called a two-parameter problem, and when the anisotropy-factor also in unknown it is called a three-parameter problem.

Both the transport theory and the Monte Carlo simulations can be used for theoretical and simulated solutions of inverse problems. One way of measuring the optical properties of a sample is by using the integrating sphere method.

2.1.3 Monte Carlo Simulations

Monte Carlo simulations are often used to simulate the light propagation in tissue, or other scattering and absorbing media. It is a statistical model based on random walk and transport theory. When simulating light transport in tissue the photons can either be scattered or absorbed. If absorbed the photon is terminated, but if scattered the photon gets a new, randomly distributed direction and then there is a chance that it will be absorbed or scattered again. In this way the program traces all the photons through the media, and the probability for scattering and absorption is given by the scattering and absorption coefficients. This is a very good model for simulating light transport in tisue, but the main disadvantage with it is the demands on fast computers [11]. In order to get good statistics, many photons are needed, and when the absorption and scattering coefficients are high the depth at which good statistics can be achieved decreases.
In Monte Carlo simulations the photons are concidered as neutral particles, and all wave phenomena are neglected. The simulation depends on the pathlength before every scattering event, as well as the absorption- scattering- and anisotropy coefficients. One of the main advantages is that the Monte Carlo model can be used even for very complex geometries [12].
In figure 2.4 the penetration depth of light at different wavelengths in tissue is illustrated. The optical properties of tissue varies with the wavelength, causing different penetration depths for light in the UV region and for light in the visible region.

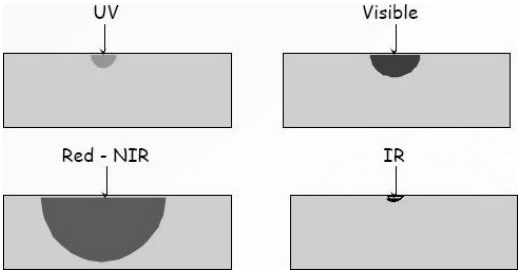

Figure 2.4: In this figure the penetration depth of light at different wavelengths in tissue is illustrated [7].

2.2 Photodynamic therapy and photosenzitizers

Photodynamic therapy (PDT) is a fairly new, non invasive, method used in clinics for treating cancer. In PDT the destruction of tumours is achieved by a photochemical reaction taking place in the tumour cells [13][14]. This reaction occurs when the tissue is irradiated with a wavelength corresponding to the absorption spectra of the photosensitizer used.

2.2.1 The photosensitizer

An often used photosensitizer is aminolevulinic acid, ALA, a precursor to haem. From ALA protoporphyrin IX is produced in the haem-cycle. Since tumour cells have a much higher metabolism they will produce more PpIX at a much higher rate than normal healthy cells. Pp IX is a light sensitive substance, that will emit fluorescence when illuminated with light at the wavelength 405 nm [15].
This can be used for diagnostic purposes, and serves as a complement to the trained eye when it comes to determine the size and location of a tumour. Pp IX is also photochemically active, which means that it will react with the oxygen in the cells when illuminated with light at the wavelength 633 nm. When illuminated, the oxygen is transformed into singlet oxygen, which is a free-radical. Free oxygen radicals are highly ractive and will destroy almost everything they come in comtact with, leading to cell death.
Since there are much more PpIX in the tumuor cells this substance can be used for targeting and killing cancer cells selectively. In this process PpIX is transferred back to its ground state, while the oxygen takes part in the toxic chemical oxidation process [15].

2.2.2 PDT treatment

Today PDT treatment is used in clinics mainly to treat superficial carcinomas with topically applied photosensitizers. One of the main problems with the treatment is the lack of information about the depth of the effective treatment. When treating thicker or deeper lying tumours information about how deep the sensitizer reaches and how deep the laser penetrates is crucial.
Since PDT almost exclusively harm the cancer cells, it is an ideal treatment of lesions where it is important not to harm the surrounding area. Skin lesions that has been treated with PDT heal fairly quick, it takes a few weeks, and it is rare to over-treat such lesions [15].
In Lund, delta-aminolaevulinic acid (ALA) is the main sensitizer used for PDT, and the laser light used for treatment has a wavelength of 633 nm.
ALA can be given orally, intravenously or it can be topically applied to the skin. When ALA is topically administrated the rest of the skin will not be light sensitive. However, the sensitizer might not reach very deep, which calls for precaution when treating deep lesions.
In resent years PDT treatment has been further developed, making it possible to treat tumours inside the body. This technique is called IPDT (Interstitial PDT) [16].

2.3 Doppler techniques

Doppler techniques have been used in many different areas within medicine, including laser-Doppler and ultrasound Doppler measurements.
Since the velocity of light is much faster than the sound velocity, slightly different methods are needed when extracting information from the Doppler shifted signal [17].
When a wave is incident on a particle it can be scattered. If the particle also is propagating in a direction, the scattered wave can experience a frequency shift. This frequency shift is known as the Doppler shift (2.13)

$$f_s = \frac{1}{2\pi}(k_s - k_i)v_s \tag{2.13}$$

where f_s is the frequency shift, v_s is the velocity of the scatterer k_s and k_i are the wave vectors of the scattering and incident waves, respectively.
As can be seen by equation (2.13), the frequency is shifted by an amount proportional to the magnitude of the velocity of the scatterers.
When refering to Doppler shifts, the terms *red shifted* and *blue shifted* light is often mentioned. The term red shifted means that the light is shifted towards longer wavelengths, and the term blue shifted means that it is shifted towards shorter wavelengths [17].
By detecting the Doppler shift it is possible to extract information about the moving particle or the incident light.
When measuring flow with a Doppler technique, there are a few important aspects to consider, and one of them is the Doppler angle. The frequency shift that arises when light interacts with moving scatterers in the material is also of interest. If the angle between the incident light and the stream of moving particles, the Doppler angle, is known then the velocity and direction of the particles can be calculated from the measured shift.

2.3.1 The Doppler angle

The Doppler angle, that is the angle between the incident laser beam and the moving scatterers (see figure 2.5), is important since it is essential in the extraction of the velocity direction of the scatterers. With most systems a fixed Doppler angle is a must when measuring the exact velocity of the flow. A 90° Doppler angle will not give rise to any frequency shift since the light has normal incident on the direction of movement, and when the Doppler angle is 180° or 0° maximal signal will be achieved since the light moves in the same, or opposite, direction as the particles, respectively.

2.3.2 Velocity measurements

When measurig the velocity of moving scatterers with laser Doppler techniqe, the Doppler equation, (2.14), is often used. It gives the relation between the mean velocity of the scatterers, V_s, and the resulting Doppler shift, f_s, at the center wavelenght, λ_0, and with refractive index, n_t, of tissue or blood [18].

$$V_s = \frac{f_s \lambda_0}{2 n_t cos\theta} \tag{2.14}$$

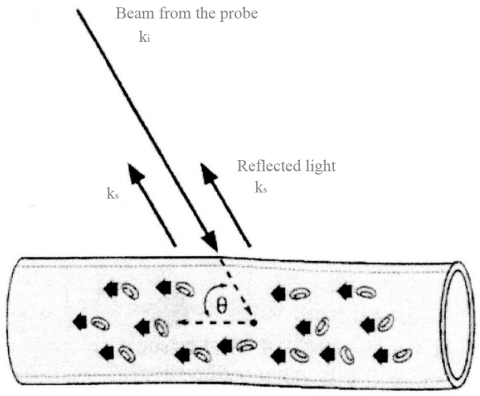

Figure 2.5: In this figure the Doppler angle is illustrated. The light beam incident on the vessel is scattered by the moving blood cells and the reflected part of the light is frequency shifted. The angle between the direction of movement for the scatterers and the incident light, θ, affects the size of the Doppler shift [19].

As seen in figure 2.5 the direction of the scatterers will determine whether the backscattered light will be shifted towards lower- or higher frequencies (red or blue shifted).
If the Doppler angle is known, as well as the refractive index of the tissue and the Doppler shifted frequency, then the velocity of the moving scatterers can also be determined.
The exact velocity of the moving scatterers is often not possible to determine, since it is hard to determine the Doppler angle for flows in tissue.

Simultaneous measurements of flow velocity and Doppler angle It is possible to measure both the Doppler angle and the velocity of the moving scatterers simultaneosly by Doppler spectrum analysis, [20].
In this way both the longitudinal and transverse components of the flow velocity can be extracted, and from that the Doppler angle as well as the velocity of the moving scatterers can be determined.
The two velocity components are determined by detecting the Doppler shift and the Doppler bandwidth.
The longitudinal and transverse velocity components are:

$$V_{longitudinal} = V cos(\theta) \tag{2.15}$$

$$V_{transverse} = V sin(\theta) \tag{2.16}$$

respectively, where θ is the Doppler angle.

Chapter 3

Optical Coherence Tomography

In 1991 the first Optical Coherence Tomography system was developed and its purpose was to build tomographic images, i.e. two- or three dimensional images, of internal structures in materials [21].
Today OCT systems can perform high resolution, cross-sectional tomographic imaging of the internal microstructure in materials by measuring on backscattered light. The imaging method is similar to ultrasound B-mode imaging [22], with the difference that OCT uses laser light instead of sound.
Today the applications of OCT spans over a wide range of fields in medicine such as opthalmology [23], retinopathy [24] and tissue diagnostics [25] - [29].

3.1 Optical Coherence Tomography

3.1.1 Ultrasound and OCT

Ultrasound measurements have been used for imaging of internal structures in materials for a long time, and with the developement of electrical and computational techniques the ultrasound imaging systems have developed further.
Although ultrasound is a great imaging tool, there are some drawbacks, for example, in order to make ultrasound measurements the transducer probe has to be in direct contact with the material. This can cause problems when performing imaging in the industry and discomfort for patients when using ultrasound for diagnostic purposes, especially when it comes to opthalmological treatments.
OCT imaging is a non invasive method based on measurements on backscattered and backreflected light, whereas ultrasound imaging is based om measurements on backscattered and backreflected sound. The dimensions of the structures can be determined by the time it takes for the echo to be backreflected at various different axial distances. Since light travels much faster than sound, the distance to the scatterers in OCT imaging has to be determined in other ways than in ultrasound imaging. There are also differences in resolution and penetration depth between OCT and ultrasound. Depending on frequency ultrasound can penetrate much deeper than light, but due to the size of the wavelengths the resoultion of OCT systems are better [30].

Waves traveling through tissue will be attenuated according to Beer-Lambert's law [3], see equation (3.1). This is one of the main limiting factors for ultrasound measurements. However, the attenuation varies with frequency, so by changing the frequency of the sound, different depths can be achieved.

$$I = I_0 e^{-\mu z} \tag{3.1}$$

where I_0 is the initial intensity, I is the intensity, μ is the attenuation and z is the distance traveled. Ultrasound echos are obtained from interference between structures with different acoustic impedance, and from non homogenous structures resulting in scattered ultrasound waves.
In ultrasound imaging the amplitude of the echo provides information on the structure in the imaged material. Structures with impedance that differs much from the surrounding material yields clearer signals, while structures with higher scattering gives a more diffuse signal. When measuring the amplitude of the echo as a function of depth, the imaging mode is called A-mode. Information on the location of the structures can be determined by equation (3.2).

$$\Delta T = \frac{z}{v} \tag{3.2}$$

Where ΔT is the echo delay, z is the distance the echo travels, i.e. twice the distance between the detector and the reflecting structure, and v is the velocity [22]. Since the velocity of light is much higher than the sound velocity the echo time delay for light can not be measured in the same way as the echo delay for sound.
The longer a pulse travels in tissue the more damped it will be, which means that the echos from deeper lying structures will be much weaker than the echoes from the structures closer to the trancducer. In order to compensate for that, signals arriving later to the detector will be amplified, which also lowers the demands on the dynamic range of the ultrasound system.
In figure 3.1 the difference in resolution between a ultrasound imaging system and an OCT system is shown.

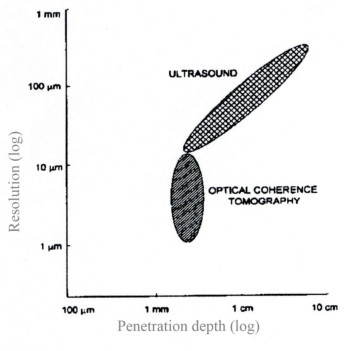

Figure 3.1: In this figure the difference in resolution between ultrasound systems and OCT systems is shown [30].

3.1.2 Measuring optical echoes

Interferometric detection techniques can be very useful when measuring ultrafast optical echoes, since it enables the detection of backreflected or backscattered light with high dynamic range and high sensitivity. Since the echo times of the light in OCT systems are extremely short a Michelson interferometer with a scanning reference delay arm and a low-coherent light source is used to obtain the depth resolution. Low coherence interferometry measures the field of the optical beam rather than its intensity.
The electric field in a light wave can be written as [30]:

$$E_0(t) = E_1 cos(\omega t - kr) \tag{3.3}$$

Where $\omega = 2\pi\nu$ is the angular frequency, r is the coordinates of the light wave, $k = \frac{2\pi}{\lambda}$ is the wave vector pointing in the direction of propagation and t is the time.
In a Michelson interferometer, see figure (3.2), the light from the source is divided into two beams by a beamsplitter; one reference beam, $E_r(t)$, that is reflected in the reference mirror and then travels to the detector, and one sample beam, $E_s(t)$, that is reflected from the sample and travels to the same detector. The light travels the distance l_r, reference length, and l_s, sample length, respectively. At the detector the fields of the two beams recombine and an interference pattern is created. The output of the interferometer is the sum of the electromagnetic fields, see equation (3.4), measured as intensity by the detector.

$$E_0(t) \sim E_r(t) + E_s(t) \tag{3.4}$$

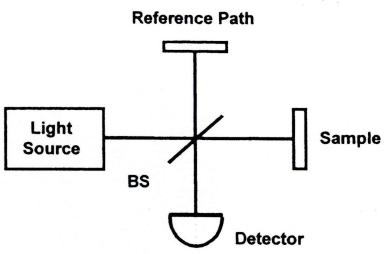

Figure 3.2: In this figure the Michelson interferometer is illustrated. The light beam is divided in two by the beamsplitter and the two beams travel in different arms of the interferometer. One beam travels to a mirror and back to the detector, while the other beam travels to a sample and then the reflected light travels back to the detector. The two beams are mixed before the detector and an interference pattern is achieved.

The intensity signal measured by the detector, see equation (3.5), is proportional to the square of the electromagnetic fields, [31].

$$I_0 \sim \frac{1}{4}|E_r|^2 + \frac{1}{4}|E_s|^2 + \frac{1}{2}E_r E_s cos(2\frac{2\pi}{\lambda}\Delta l) \tag{3.5}$$

When the position of the reference mirror is varied the resulting interference pattern vill also vary, yielding information on the distance from the source to

the reflection in the sample. Interference is only observed when the difference in pathlength between the reference arm and the sample arm, $\Delta l = l_r - l_s$, is less than the coherence length of the source, l_c, which is inversely proportional to the bandwidth of the source. By using a low coherence light source in the OCT system absolute distances and small internal structures can be imaged, which is necessary for many applications.
Low coherence light can be seen as a superposition of electromagnetic fields with statistical discontinuities in phase as a function of time. This means that the field consists of different frequencies and wavelengths, rather than one. The difference between light with short coherence length and light with long coherence length is illustrated in figure (3.3).

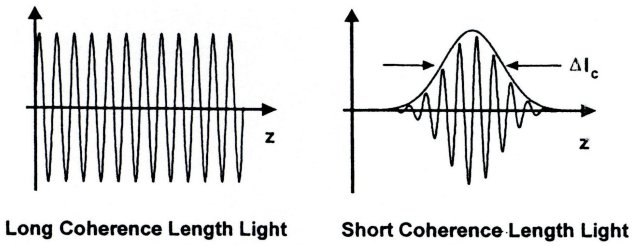

Figure 3.3: In this figure the difference between light with short coherence length and light with long coherence length is illustrated. The left hand figure shows light with long coherence length and the right hand figure shows light with short coherence length. The coherence length of the light is given by the full width at half maximum, FWHM, as illustrated in the right hand figure [30].

The interferometer measures the autocorrelation of the light, and the coherence length determines the resolution with which the optical range or distance can be measured. By scanning the reference arm and demodulating the interference signal, the echo time and delay can be determined.

3.1.3 Resolution and sensitivity

In OCT the axial and transverse image resolution are independent, in contrast to ordinary confocal microscopy.
The axial resolution in an OCT system is determined by the coherence length of the light source. This means that high axial resolution can be achieved independently of the beam-focusing conditions. The coherence length is the spatial width of the field autocorrelation produced by the interferometer. The envelope of the field autocorrelation is equivalent to the Fourier transform of the power spectrum. Thus, the width of the autocorrelation function, or the axial resolution, is inversely proportional to the width of the power spectrum. The axial resolution, Δz, for a source with a Gaussian spectral distribution is given by equation (3.6).

$$\Delta z = \frac{2ln2}{\pi}\left(\frac{\lambda^2}{\Delta\lambda}\right) \tag{3.6}$$

Where Δz and $\Delta\lambda$ are the full width at half-maximum (FWHM) of the autocorrelation function and power spectrum, respectively, and λ is the source

center wavelength [32]. The axial resolution is inversely proportional to the bandwidth of the light source, and thus broad-bandwidth optical sources with a Gaussian shape are required to achieve high axial resolution.
When using a Gaussian shaped source the analysis of the Fourier transformed signal will be easier since the Fourier transform of a Gaussian shape is a Gaussian shape, in contrast to a rectangular shape that, after Fourier transformation, will have a sinc-shape.
The transverse resolution for OCT systems are the same as for ordinary optical microscopy, i.e. it is determined by the focusing properties of the optical beam. The minimum spot size to which a beam can be focused is inversely proportional to the numerical aperture of the angle of focus of the beam. The transverse resolution is given by equation (3.7) [33].

$$\Delta x = \frac{4\lambda}{\pi}(\frac{f}{d}) \tag{3.7}$$

where d is the spot size on the objective lens and f is its focal length. High transverse resolution can be obtained by using a large numerical aperture and focusing the beam to a small spot size. In addition, the transverse resolution is also related to the depth of focus or the confocal parameter b, which is $2z_R$, two times the Rayleigh range, see equation (3.8) [34].

$$2z_R = \frac{\pi \Delta x^2}{2\lambda} \tag{3.8}$$

Thus, increasing the transverse resolution produces a decrease in the depth of focus, similar to that produced in conventional microscopy.

Optical coherence tomography can achieve high detection sensitivity because interferometry measures the field rather than the intensity of the light using optical heterodyne detection. The oscillating interference term in the intensity equation, (3.5), is the result of the backscattered or backreflected electric field from the sample multiplied by the electric field of the reference beam. Because the beam from the reference arm can have a large field amplitude, the weak electric field from the sample is multiplied by the large field amplitude, thereby increasing the magnitude of the oscillating term that is detected by the detector. The interferometer thus produces heterodyne gain instead of weak optical signals.
Backreflected or backscattered optical echoes from the specimen are detected by electronically demodulating the signal from the photodetector as the reference mirror is translated. In most OCT embodiments the reference mirror is scanned at a constant velocity, v, that Doppler shifts the reflected light. This modulates the interference signal at the Doppler beat frequency:

$$f_D = \frac{2v}{\lambda} \tag{3.9}$$

Where v is the reference mirror velocity.

By electronically filtering the detected signal at this frequency, the presence of echoes from different reflecting surfaces in the biological specimen may be detected. In addition, it is interesting to note that if the light is backreflected or backscattered from a moving structure, it will also be Doppler shifted and

result in a shift of the beat frequency. This has been used to perform OCT imaging with additional Doppler measurements of flow.

3.1.4 Image generation

Optical coherence tomographic cross-sectional imaging is achieved by performing successive axial measurements of backreflected or backscattered light at different transverse positions.
A two-dimensional cross-sectional image is aquired by scanning the incident optical beam, performing successive rapid axial measurements of optical backscattering or backreflection profiles at different transverse positions. The result is a two-dimensional data set in which each trace represent the magnitude of reflection or backscattering of the optical beam as a function of depth in the tissue.
The most common method of OCT scanning aquires data with depth priority. However, it is also possible to aquire data with transverse priority, by detecting backreflections or backscattering at a given depth or range while transversely scanning the imaging beam.
When performing OCT imaging in highly scattering media, such as tissue, the detection sensitivity is limiting the maximum depth. Thus, reducing the scattering is important, and that can be achieved by using longer wavelengths, in the order of 1300 nm. This is important, since the contrast for OCT imaging is determined by the attenuation both from the absorption and scattering that will occur when the light propagate to the structure from which it will be reflected, and then the attenuation of the backscattered light that will be imaged.

3.2 Doppler Optical Coherence Tomography

Different techniques have been developed in order to measure blood flow in tissue. One of the first techniques was Doppler ultrasound, which measures the Doppler shift of sound waves reflected from moving particles in order to determine their velocities [35].
Doppler-optical coherence tomography (DOCT) is a fairly new method for monitoring blood flow in tissue. It is based on Optical Coherence Tomography (OCT), and by measurements on the interference fringes of the backscattered light the location of scattering structures can be determined as well as their velocity [27].
In ordinary OCT imaging the scanning reference mirror gives rise to a Doppler shift in the reflected light, which modulates the interference signal at the Doppler beat frequency, f_D. If, in addition, the light is backscattered from a moving structure, yet another Doppler shift will occur, resulting in a shift of the beat frequency. By detecting this shift information on the velocity of the moving scatterers can be extracted.
Since DOCT is based on a Michelson interferometer, the interferometric cross-correlation, $\tilde{R}_{is}(\Delta l)$, between sample and reference arm as a function of the pathlength difference between the two arms, Δl, can be determined [30].

$$\tilde{R}_{is}(\Delta l_g, \Delta l_\phi) = R_{is}(\Delta l_g) e^{-ik_o \Delta l_\phi} \tag{3.10}$$

where k_0 is the center wavenumber of the optical source and Δl_ϕ and Δl_g are the phase and group delays, respectively, expressed as pathlength differences

[36]. As can be seen in equation (3.10), R_{is} is purely a function of the group delay, while the carrier frequency is determined by the phase delay.
With a Fourier Rapid Scanning Optical Delay line, RSOD, the group and phase delays can be controlled independently [37].

$$\Delta l_\phi = 4\sigma x_0 \tag{3.11}$$

$$\Delta l_g = 4\sigma x_0 - \frac{4\sigma l_f \lambda_0}{p} \tag{3.12}$$

where σ is the angle of the resonant mirror in the reference arm, λ_0 is the center wavelength, x_0 is the offset of the light on the mirror resulting from the tilting, l_f is the focal length and p is the pitch of the grating used in the Fourier RSOD. The center frequency of the carrier of the interferogram, see equation (3.14), can be obtained with help of the scan speed of the phase delay, V_ϕ.

$$V_\phi = \frac{d\Delta l_\phi}{dt} \tag{3.13}$$

$$f_0 = \frac{V_\phi}{\lambda_0} = \frac{4x_0}{\lambda_0}\frac{d\sigma(t)}{dt} \tag{3.14}$$

The movement of a scatterer will give rise to another Doppler shift on the center frequency of the signal, and it can be estimated to [38]:

$$\bar{\omega} = \frac{\int_{-\infty}^{\infty} \omega P(\omega) d\omega}{\int_{-\infty}^{\infty} P(\omega) d\omega} \tag{3.15}$$

with help of the centriod of the power spectrum, $\bar{\omega}$. This frequency shift can also be written as:

$$\bar{\omega} = \frac{4\pi V_s n_t cos(\theta)}{\lambda_0} \tag{3.16}$$

where n_t is the refractive index of the sample and θ is the angle between the incident light and the direction of the moving scatterers, V_s. The autocorrelation function, $R(\tau)$ is, according to the Weiner-Khinchin theorem, the inverse Fourier transform of a power spectra [36].

$$R(\tau) = \int_{-\infty}^{\infty} P(\omega) e^{i\omega\tau} d\omega \tag{3.17}$$

where τ is the delay of the autocorrelation. If equation (3.17) and its first derivative with respect to τ is inserted into equation (3.15) and the result is evaluated at $\tau = 0$, the centroid can be expressed as [39]:

$$\bar{\omega} = i\frac{\frac{d}{dt}R(0)}{R(0)} \tag{3.18}$$

This expression gives $\bar{\omega}$ in the time domain, but it is still difficult to calculate $\frac{d}{dt}R(0)$ in real-time. To solve this problem the phase and group delay can be rewritten as functions of time:

$$\tilde{i}_{is} = \rho R_{is}(\Delta l_g(t)) e^{-ik_0 \Delta l_\phi(t)} = g(t) e^{i(\omega_r + \omega_s)t} \tag{3.19}$$

where the group delay defines the envelope and the frequency shifts in the interferometer arms, ω_r and ω_s, gives the carrier frequency, and where $\tilde{i}_{is}$ is the

interferometric current proportional to $\tilde{R}_{is}(\Delta l)$.
Taking the real part of the complex signal yields [36]:

$$\tilde{g}(\omega_g, t) = g(t)sin(\omega_g t) \tag{3.20}$$

with the carrier frequency written as $\omega_g = 2\pi(f_r + f_s)$.
A constant amplitude of the envelope can be achieved by using a high dynamic range limiter. By correlating two A-scans, one shifted 90°, f_s can be extracted.

$$\tilde{g}_n(\omega_g, t) = g \cdot sin(\omega_g t + \pi/2) \tag{3.21}$$

with the interferogram of the previous A-scan:

$$\tilde{g}_{n-1}(\omega_g, t) = g \cdot sin(\omega_g t + \vartheta_{n-1}) \tag{3.22}$$

Where instabilities in the interferometer is represented by ϑ_n, a random phase noise term [36].
With this done, the autocorrelation can be written as [36]:

$$\tilde{R}_{\tau_{scan}} = \langle \tilde{g}_n(\omega_g, t) \cdot \tilde{g}_{n-1}(\omega_g, t + \tau_{scan}) \rangle \tag{3.23}$$

By inserting (3.21) and (3.22) into (3.23) and using a trigonometric identity the autocorrelation function can be written as:

$$\begin{aligned} \tilde{R}_{\tau_{scan}}(\omega_g) = -\frac{1}{2}g^2 \langle cos[\omega_g(2t + \tau_{scan}) + \pi/2 + \vartheta_{n-1}] \rangle \\ + \frac{1}{2}g^2 cos[\omega_g \tau_{scan} + \pi/2 - \vartheta_{n-1}] \end{aligned} \tag{3.24}$$

The expected value of the first term in the above expression, (3.24), is zero, and the second term simplifies to:

$$\tilde{R}_{\tau_{scan}}(f_s) \propto -sin(2\pi f_s \tau_{scan} - \vartheta_{n-1}) \tag{3.25}$$

taking into consideration $\omega_g = 2\pi(f_r + f_s)$ and $f_r \tau_{scan} = Integer$. As seen in equation (3.25), the function $\tilde{R}_{\tau_{scan}}(f_s)$ will vary sinusoidally as a function of the Doppler shift, f_s in the sample when the interferometer is sufficiently stable, i.e. when $\vartheta_n \ll 2\pi$ [36].
The A-scan aquisition rate, $f_{scan} = 1/\tau_{scan}$, affects both the monotonic range, given by $\pm f_{scan}/4$, and the flow sensitivity. Higher aquisition rates gives lower sensitivity. Rings will appear in the images when the flow is higher than the monotonic range due to the sinusoidal variations in the autocorrelation function.

There are certain limitations on the detectable flow velocities, and the phase noise is the limiting factor when it comes to the minimum detectable flow according to equation (3.26).

$$V_{min} \geq \frac{\lambda_0 f_{scan}}{2n_t cos(\theta)} \cdot \frac{\vartheta_{n-1}}{360°} \tag{3.26}$$

The upper limit is set by the moving scatterers, the focal length and the coherence length of the source according to the following equation [36]:

$$V_{max} \leq \frac{1}{2} \cdot \min \left[\frac{\oslash_{beam}}{sin(\theta)}, \frac{l_c}{cos(\theta)} \cdot \frac{1}{\tau_{scan}} \right] \tag{3.27}$$

Where the moving scatterers has to remain axial and lateral within the coherence length, l_c, and focal region of diameter $\oslash_{beam}$ for at least τ_{scan}.

3.3 The DOCT system from Risø

The Optics and Plasma Research department at Risø National Laboratory in Denmark has recently developed a Doppler-OCT system that utilizes a grating-based rapid scanning optical delay line, (RSOD).
The computational algorithm used in this Doppler-OCT system is called Field Programmable Gate Array, FPGA, and it is used to digitally process the Doppler-OCT signals.

3.3.1 System setup

In figure 3.4 a schematic image of the DOCT system is illustrated. This Doppler OCT system works at the wavelenght 1300 nm and utilizes a semicomductor laser. By using a broad, low coherent light scource, good resolution and a gate window is achieved.
The light is led from the scource, through optical communication fibres, to an

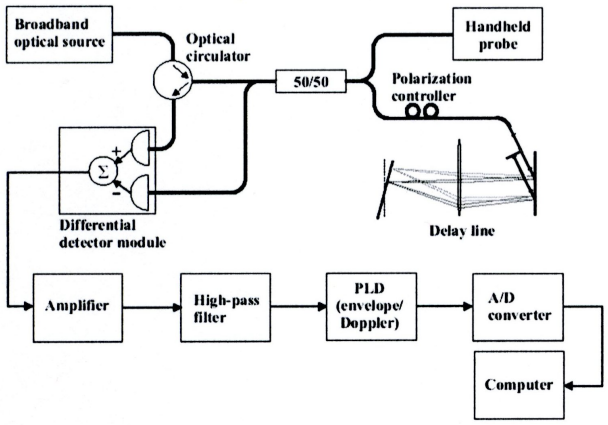

Figure 3.4: In this figure a block diagram of the Doppler Optical Coherence Tomography system is illustrated [19]. The light is emitted from the source, through optical fibres, to an optical circulator and from there one part is led to a beamsplitter and one part to a differential detector module. From the beamsplitter one part of the light is led to a reference scanner and the other part to the handheld probe and from that to the sample. The two signals are then led through an optical delay line and to the detector.

optical circulator and from there, one part is led to a beamsplitter and one part to a differential detector module. In the beamsplitter the light is divided into two fibres and half of the light goes into one of the fibres and is led to a reference scanner, while the other half is led to a handheld probe and from there to the sample.
The reference scanner is swept back and forth and an interference pattern is created when the signals from the reference scanner is mixed with the signal from the sample. The two signals are mixed after having gone through an optical delay line. The detected signal is led to an amplifier and further to a high-pass

filter.
The grating based optical delay line is constructed to compensate for the fact that different wavelengths experience different angles when diffracted at a grating or reflected in a mirror.
In the set up a galvano-scanner is rotating a mirror so that four sequential A-scans can be performed. The sequential A-scan model helps in reducing the noise since it is performing several scans in the same point, and that can be used for eliminating the fluctuating noise. When the signal reaches the computer several computational algorithms are used before an image is presented on the screen.
In figure 3.5 pictures of the Doppler-OCT set up is shown.

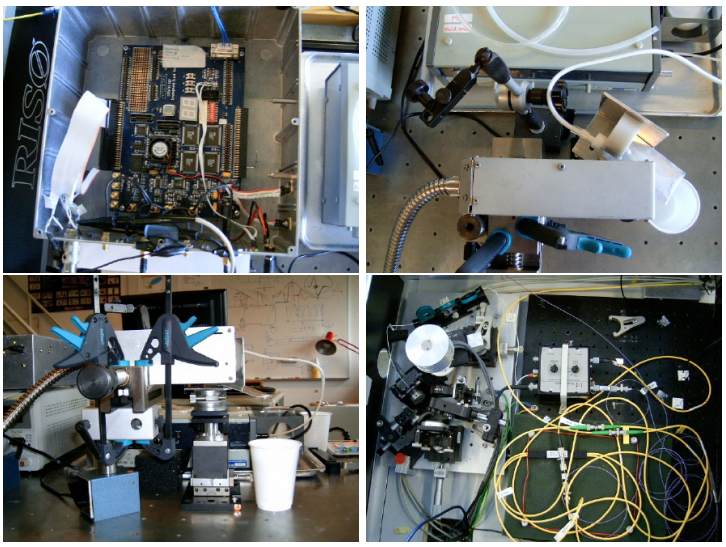

Figure 3.5: In this figure pictures of the Doppler-OCT set up are shown. Upper left hand image shows the Altera board where some of the calculations are performed. The upper right hand image shows the phantom mounted close to the probe. The lower left hand image shows the probe mounted in a holder to prevent movements. The lower right hand image shows some of the optical fibres and the scanner inside the actual DOCT system.

3.3.2 Field Programmable Gate Array, (FPGA)

This system uses an FPGA in a grating-based rapid scanning optical delay line. This solution enables sampling rates that exceedes the ones of the old Digital Signal Processing, DSP, unit [40].
A field programmable gate array, FPGA, is an array of logical building blocks and a connective network. It is a chip that can be programmed using the language VHDL, VHSIC (Very High Speed Integrated Circuit) Hardware Description Language.
In this implementation an FPGA that looses the memory when the current is removed has been used. Since the light from the hand held probe is reflected in tissue without any clear reflection, there is a need for extensive filtering in

order to extract the backscattered or backreflected signal.
The design of the new DSP, see figure 3.6, that is used in this Doppler-OCT system will be briefely decsribed below. The OCT signal is divided in two parts.

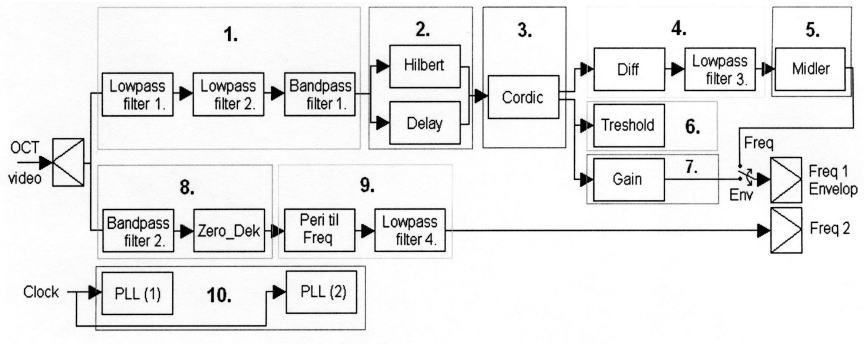

Figure 3.6: In this figure a schematic image of the new DSP design is shown [19].

One part is led in to a filter section with two lowpass and one bandpass filter. The signal is then subdivided into two signals. One of those signals goes into a Hilbert filter, while the other goes into a delay line in order to match the group delay of the Hilbert transformed signal. When those signals are matched, they are led into a CORDIC, Cordinate Rotation Digital Computer, algorithm [19] where the complex rectangular OCT signal is converted into a polar form.
From the CORDIC algorithm there are two signals coming out and one is led into a lowpass filter and from that into an algorithm that computes the frequency that will be transmitted to the computer. The other signal from the CORDIC algorithm is further divided in two, one being used to check that the amplitude of the signal is above the noise level, while the other is scaled to fit the A/D converter.
The OCT signal was initially divided in two and while one of the parts were led into a chain of filters and algorithms designed to extract the frequency and the envelope, the other part is led into a series of filters in order to extract the Doppler frequency. The first filter is a bandpass filter followed by a zero-detection algorithm. The output from this combination gives the number of samles per period for the OCT signal. The signal is then converted to frequency and filtered again to reduce the noise.

3.3.3 The effect of the Doppler angle

As described in section 2.3 the Doppler angle substantially effects the velocity measurements. If the angle between the incident laser beam and the moving scatterer is 90° there will be no Doppler shift due to the movement of the scatterer and hence the velocity cannot be extracted. If the Doppler angle is unknown neither the velocity nor the direction of the moving scatterers can be determined.
The frequency shift of the backscattered light will vary depending on the size of the Doppler angle. A large angle will give rise to a small frequency shift of the signal, while a small Doppler angle will give a large Doppler shift, see figure

(3.7). This relation can also be described by the following equation:

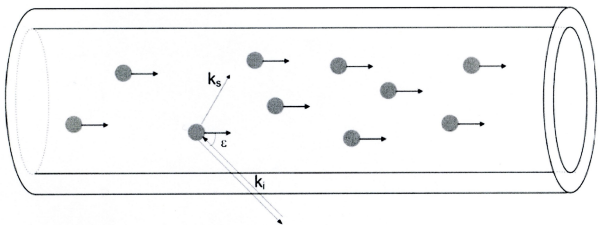

Figure 3.7: In this figure the Doppler angle, i.e. the angle between the incident laser beam and the moving scatterer is illustated.[41]

$$f_s = \frac{1}{2\pi}(k_s - k_i)v_s \tag{3.28}$$

where f_s is the Doppler shifted frequency v_s is the velocity of the scatterers k_i and k_s are the incident and scattering wave vectors, respectively and λ_0 is the center wavelength.
If the incident wave and the scattered wave reside in the same plane, equation 3.28 can be written as:

$$f_s = \frac{2nv_s sin\left(\frac{\Psi}{2}\right) sin\left(\epsilon + \frac{\Psi}{2}\right)}{\lambda_0} \tag{3.29}$$

where n is the refracive index, Ψ is the angle between the incident wave and the reflected wave and ϵ is the angle between the velocity vector and the flow.
If only the backscattered light is detected, as in the case of DOCT, then $k_s = -k_i$ and $\Psi = 180°$ and equation 3.29 will simplify to:

$$f_s = \frac{2nv_s cos(\epsilon)}{\lambda_0} \tag{3.30}$$

By decreasing the angle between the beam and the moving scatterers, lower flows can be detected within the same algorithm.

Chapter 4

Laser Doppler blood Flowmetry

In 1972 the first *in vivo* study of blood flow based on Doppler broadening of coherent light was presented [42], and in 1975 the first *in vivo* skin perfusion measurements were described [43].
Since then the techniques have developed, and several important refinements have been presented, e.g. the non-contact imaging technique [44] [45] and the differential detector technique [46].
Other thorough rewiews describing light scattering in tissue, signal generation and perfusion estimate have also been presented [47] - [52].

4.1 Laser Doppler blood Flowmetry

In LDF coherent light generated by e.g. a HeNe laser or a diod laser is used to illuminate the tissue, and the backscattered light is detected by a photodetector at the tissue surface, see figure (4.1). Part of the light incident on the tissue will be reflected at the surface and the rest will be scattered and absorbed due to the different tissue constituents. Scattering can occur in static structures such as cell kernels and membranes, but the light can also be scattered by moving objects such as red blood cells. When this happens the light will undergo a Doppler shift according to equation (2.13). Since the velocity of the blood cells in the capillaries in the skin is very small the resulting Doppler shift will also be small, and impossible to detect with ordinary spectroscopic methods.

Scattering events Light incident on tissue will be scattered and absorbed due to the tissue constituents and structure. When light is scattered by moving objects the frequency will change according to the Doppler principle.
A wave, E_i, propagating in the direction k_i can be written as:

$$E_i = E_{i0} e^{i(\omega t + k_i r)} \tag{4.1}$$

where E_{i0} is the amplitude, r represents the spatial coordinates, t is the time and ω is the angular frequency. After a scattering event the wave can be written as:

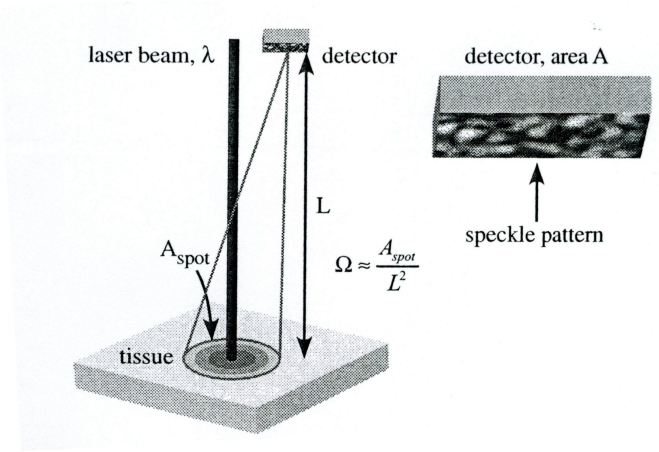

Figure 4.1: In this figure the LDF set up is illustrated. The reflected laser light causes a speckle pattern on the detector surface. The size of the coherence areas on the detector is dependent on the distance from the sample to the detector and on the solid angle from which the light spot is seen from the detector [53].

$$\begin{aligned} E_s &= E_{so} e^{i((\omega - k_i v)t - k_i r_0 - k_s(r_1 - vt))} \\ &= E_{so} e^{i\omega t} e^{-i(k_i - k_s)vt} e^{-i(k_i r_0 + k_s r_1)} \end{aligned} \tag{4.2}$$

where E_{so} is the amplitude of the scattered wave, v is the particle velocity and $e^{-i(k_i r_0 + k_s r_1)}$ is a time-invariant phase factor. By neglecting the time-invariant phase factor equation (4.3) simplifies to [2]:

$$E_s = E_{s0} e^{i\omega t} e^{-i(k_i - k_s)vt} \tag{4.3}$$

For further simplification the scattering vector, $q = k_i - k_s$, can be introduced. As seen in equation (4.3) the wave will only be frequency shifted if the scattering object is moving and if the angle between the object and the wave is $\theta \neq 90°$. The magnitude of the scattering vector can be written as:

$$q = 2ksin\left(\frac{\alpha}{2}\right) = \frac{4\pi}{\lambda} sin\left(\frac{\alpha}{2}\right) \tag{4.4}$$

where α is the scattering angle and λ the wavelength. This gives the angular Doppler frequency ω_D [2]:

$$\omega_D = \frac{4\pi}{\lambda} sin\left(\frac{\alpha}{2}\right) vcos(\theta) \tag{4.5}$$

Signal detection and processing In order to resolve the small Doppler shift generated by the light interaction with moving scatterers, detection techniques such as heterodyne detection [54] have to be applied.
In heterodyne detection one field centered around a frequency f_1 and an oscillating field centered around another frequency f_2 are mixed and the new field

is detected. This new field that arises will have a center frequency of $|f_1 - f_2|$. By detecting this frequency and comparing it to the frequency of the light incident on the tissue the frequency shift generated by the moving scatterers can be extracted.
Since only a small part of the backscattered light will be Doppler shifted the light incident on the tissue can be mixed with the light detected and the frequency shift can be investigated.
A speckle pattern with temporal and spatial variations will be produced on the photodetector. The pattern arises when the backscattered light reaches the detector, and the variations are due to the Doppler shift generated by the moving scatterers. The number of moving scatterers, e.g. red blood cells, and their average velocity in the volume will affect the magnitude and frequency of the intensity signal. These signals enables calculation of the tissue perfusion [47].
The number of coherence areas, N, on the detector is given by equation (4.6).

$$N = \frac{A}{A_c} \tag{4.6}$$

where A is the area of the detector and A_c is the size of a coherence area, which is given by equation (4.7).

$$A_c = \frac{\lambda^2}{\Omega} \tag{4.7}$$

where Ω is the solid angle from which the light spot is seen from the detector.

$$\Omega = \frac{A_{spot}}{L^2} \tag{4.8}$$

The size of the coherence areas are affected by changes in the spot size A_{spot} and the distance between the detector and the tissue, according to (4.7) and (4.8).
In the photodetector the light intensity is converted to a photocurrent, $i(t)$ that is proportional to the instantaneous light intensity [2].

$$i(t) = \sum_{j=1}^{K} \big(\langle i_c \rangle + \Delta i_{cj}(t) \big) \tag{4.9}$$

Where $\langle i_c \rangle$ is the average portion of the photocurrent, and $\Delta i_{cj}(t)$ is the fluctuating part of the photocurrent produced by the coherence area j and K is the number of coherence areas on the detector surface.
With the assumption that the fluctuating parts of the photocurrent produced by the different coherence areas are independent and that the average value of those components are zero, the autocorrelation function describing the photocurrent can be written as:

$$\begin{aligned} \big\langle i(0)i^*(\tau) \big\rangle &= \sum_{j=1}^{K} \big(\langle i_c \rangle + \Delta i_{cj}(0) \big) \sum_{l=1}^{K} \big(\langle i_c^* \rangle + \Delta i_{cl}^*(\tau) \\ &= \sum_{j=1}^{K} \sum_{l=1}^{K} \langle i_c \rangle \langle i_c^* \rangle + \sum_{j=1}^{K} \sum_{l=1}^{K} \Delta i_{cj}(0) \Delta i_{cl}^*(\tau) \\ &= K^2 \big\langle i_c \big\rangle^2 + K \big\langle \Delta i_c(0) \Delta i_c^*(\tau) \big\rangle \end{aligned} \tag{4.10}$$

In equation (4.10) it can be seen that the static part of the autocorrelation function scales with the square of the number of coherence areas while the Doppler realted part scales linearely with the number of coherence areas [2].
The relation between the photocurrent produced by a single coherence area and the E-field can be written as:

$$i_c(t) \propto E(t)E^*(t) \tag{4.11}$$

or as:

$$\langle i_c(0)i_c^*(\tau)\rangle \propto \langle E(0)E^*(0)E(\tau)E^*(\tau)\rangle \tag{4.12}$$

This equation,(4.12), contains terms representing both the Doppler shifted photons, and the photons that have not undergone a frequency shift.
By further calculations the conclusion that the average current produced by photons shifted in frequency in a single coherence area is proportional to the total photocurrent produced by a single coherence area, for a moderate number of red blood cells (RBC), can be drawn.
This can be seen in equation (4.13) [2], where not only the heterodyne and the homodyne mixing is represented but also the stationary part.

$$\langle i_c(0)i_c^*(\tau)\rangle = \underbrace{2i_{Re}i_{Sc} + i_{Re}^2 + i_{Sc}^2}_{stationary} + \underbrace{i_{Re}i_{Sc}\big(\langle e^{iqvt}\rangle + \langle e^{-iqvt}\rangle\big)}_{heterodyne-mixing} + \underbrace{i_{Sc}^2\left\langle \frac{1}{S^2}\sum_{k=1,k\neq l}^{S}\sum_{l=1}^{S} e^{i(q_k v_k - q_l v_l)\tau}\right\rangle}_{homodyne-mixing} \tag{4.13}$$

A few assumptions has to be made in order to be able to link the RBC velocity distribution for a specific wavelength to the power spectral density function. The first one is that the velocity distribution is independent of the spatial coordinates, the second one is that the single RBC move independently of one another and the final assumption is that the concentration of RBC is low enough to neglect multiple scattering events.
To arrive at the power spectral density function one has to start with calculating the carrier frequency, e^{iqvt} for the three dimensional velocity distribution, $N_0(v)$. The Fourier transform of the average value of the carrier frequency with respect to the scattering vector distribution gives, according to the Weiner-Khintchin theorem, the power spectral density.

There are two different types of LDF systems, namely: Laser Doppler Perfusion Monitoring (LDPM) and Laser Doppler Perfusion Imaging (LDPI) systems. Both will be described in the following sections.

4.2 Laser Doppler Perfusion Monitoring

Laser Doppler Perfusion Monitoring, LDPM, is a method based on measurements on backscattered and back reflected light. It was the first prototype of a laser Doppler flowmeter, and in the beginning a He-Ne laser at wavelength 632.8 nm was used and the light source was placed approximately 1 m above

the sample surface.
In order to get a smaller and more stable device to work with, a system using optical fibres to guide the light to and from the sample were developed.
Today the setup consists of two, or more, optical fibres placed at the sample surface at a certain distance, d. The light is led into one of the fibres from the light source through a small lens and to the sample. The backscattered and backreflected light is then collected by the other fibre and guided to the detector surface, where it creates a speckle pattern on the detector surface. The light source is often a diode laser emitting at the wavelength 780 nm. This wavelength allows a relatively deep penetration into the tissue possible. Other wavelengths are also possible to use. With this setup, illustrated in figure 4.2, it is possible to continousely monitor the tissue perfusion at the single sight illuminated.
One of the main advantages with the LDPM system is that is can be used invasively as well as noninvasively, but a disadvantage is the small sample volume which makes the system sensitive for local variations in blood perfusion.
Since the fibres are positioned at the sample surface the temperature needs to be regulated in order to avvoid an increase or decrease in perfusion due to heating. The signal processing involves highpass filtering in order to extract the

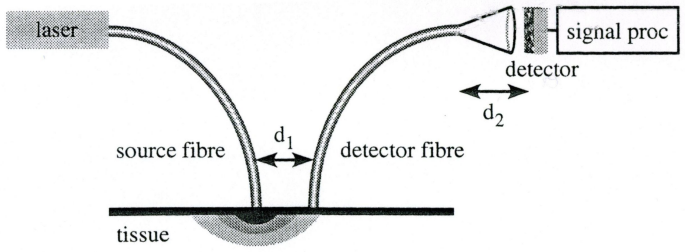

Figure 4.2: In this figure the LDPM set up is illustrated. The laser light is led to the tissue surface through a fibre and at a distance d_1 frpm the source fibre the detector fibre is placed. The light collected by the detector fibre is then led to the detector [53].

Doppler signal from the average photocurrent. To make the extracted signal independent of the light intensity it is amplified and normalized by the average photocurrent.

4.3 Laser Doppler Perfusion Imaging

Laser Doppler Perfusion Imaging, LDPI, is a technique based on measurement of the Doppler broadening of the optical spectrum that occurs when coherent light is scattered by moving particles.
There are similarities between LDPM and LDPI, both systems are based on measurement on light after interaction with, for example, tissue, but in LDPI a two-dimensional map of the perfusion is created instead of the single sight measurements that can be performed with the LDPM system.
In figure 4.3 a schematic image of the LDPI system is shown. As can be seen, the light from the source is directed on to a scanning mirror and from that to the sample. This means that the light beam will be swept over a surface in

order to extract information to build a two dimensional map over the flow. The backscattered light is reflected on the same mirror as the outgoing light and from the mirror the light is directed to the detector.
There are two ways of sweeping the light beam over the surface, one is by continousely sweeping the beam and collecting the backscattered light while moving. This method can cause movement artefacts in the perfusion calculations, but more measurement points can be collected in this way.
The other way of sweeping an area is by making a measurement in one point, move the beam a small distance and pause it there for a few milliseconds before another measurement is taken. In this way the movement artefacts can be reduced, but the measurement will take longer time and not as many measurement sites will be achieved.
In LDPI, in contrast to LDPM, the number of coherence areas changes when the distance between the surface and the detector change. This problem has been solved by using a source with a slightly divergent beam and keeping a fixed solid angle between the light spot on the tissue and the detector. The signal

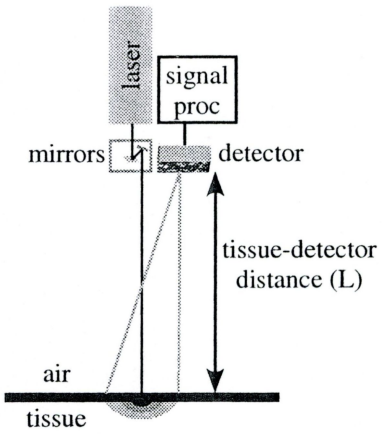

Figure 4.3: In this figure the LDPI set up is illustrated. The laser light is incident on the sample, where it is scattered and absorbed. The backscattered light is detected at a distance L from the sample [53].

processing in the LDPI system is similar to the processing in LDPM.
By monitoring the intensity of the reflected light, areas with clearly different optical properties can be extracted. If, for example, a tissue sample is placed on a highly absorbing, or reflecting, background the signal processing device can be set to separate the sample from the background.
Good signals can be achieved by adjusting the distance between the sample and the detector.
There is a possibility to use the LDPI system for monitoring as well, and when doing this the perfusion images are continousely updated.

4.3.1 High-resolution Laser Doppler Perfusion Imaging, (HR-LDPI)

Sometimes the resolution of a normal LDPI system is too low, and a modification of the set up is needed to increase the resolution.
Often the system characteristics limits the lateral resolution of a LDPI system. In order to increase the resolution of the LDPI system, the step-length can be decreased and by focusing the beam on one spot on the surface and keeping the distance between the surface and the detector constant.
In this way the solid angle between the detector and the surface can be decreased, which in turn increases the size of the coherence areas on the detector and in that way also increases the amplification factor.
The size of the images recorded will also be reduced when the step-length is reduced, unless the measurement time is increased.
If larger images is to be recorded with a High-resolution LDPI system the sample needs to be properly fixed, so that movement artefacts can be reduced.
HR-LDPI has, for example, been used for imaging of microvascular blood flow [55][56].

Chapter 5

Tissue phantoms

When it comes to making calibration measurements, and testing the resolution of a system, well defined tissue phantoms can be valuable.
In order to make realistic measurements, and good comparisons of the two flow monitoring systems, DOCT and LDPI, tissue phantoms with low flows in small tubes was to prefer. Since no such phantoms existed, they had to be produced as a part of the project.
Recipes and detailed description on how to make epoxy based tissue phantoms are given in appendix A.

5.1 Introduction to tissue phantoms

The idea behind tissue phantoms is to make something very similar to tissue. Depending on what kind of systems that are performing the measurements, different types of properties are important. Phantoms that are to be used for optical measurements have properties that differ from phantoms used for ultrasound measurements. One thing they have in common though is that they are being used for calibration.
When choosing and making phantoms for optical measurements there are mainly two parameters that are important, namely; the absorption and scattering coeffcients. By giving the phantom optical properties similar to the ones of tissue [57][58], valuable data can be produced.
There are many different types of tissue phantoms, all from liquid to hard epoxy based phantoms, and they all serve different, equally important, purposes. Tissue phantoms can even be made in different layers to simulate the layers of tissue [59] - [64]. By varying the absorption and scattering coefficients the phantoms can be adapted to fit different wavelengths, and in that way different systems.
One of the most commonly used tissue phantom materials is Intralipid, a liquid with optical properties similar to the ones of tissue. One of the main advantages with Intralipid is that it is very easy to handle, but on the other hand phantoms made of Intralipid does not last for a long time due to the evaporation of fluids and aggragation of lipid droplets.
A material that lasts longer, and is suitable for making phantoms out of, is epoxy. The disadvantage with epoxy is the process of making the phantoms, which is time consuming and not so easy, but on the other hand epoxy phantoms

can be molded into almost any shape.
Since the tissue phantoms can be made quite exact and since they are easy to control, a good set of phantoms can be very valuable when it comes to calibrating a system. Phantoms also play an important role when comparing different systems, since they do not change, like for example tissue samples do. Measurements on phantoms also serve as a good preperation for measurements on tissue.

5.2 The tissue phantom design

When making phantoms it is important to keep in mind what kind of measurement the phantoms are supposed to be used for and adapt after that. The phantoms that are suitable for one type of measurement may not be useful for another purpose.
Since the measurements in this study was aiming to measure blood flow in tissue, there was a need for tissue phantoms with integrated flows. The flows to be simulated were the ones in the capillaries in the skin, and therefore the phantoms had to be adapted to fit that. This means small tubes, in the order of μm in diameter and flows in the order of $mm/s - \mu m/s$.
The flows had to be contained close to the phantom surface, that is between 0.1-1 mm below the surface, in order to be detected by the systems. This because of the shallow penetration depth of the lasers in the systems. It is also of interest to monitor the capillaries in the skin and hence the tubes in the phantoms has to lie close to the surface in order to have a good resemblance to the skin.
In order to have phantoms that could be used over a long period, epoxy based phantoms were choosen. Those phantoms are also easy to model, and by grinding them, small distances between tube and surface can be achieved.
Since fluid is to be led through the small tubes in the phantom, a device for attatching tubes to the holes in the phantom had to be designed as well. Because of the difficulty to drill holes with small diameter over long distances, a hose attatching device was glued on to the phantom with heat activated glue.
The flow in the tubes has to be laminar, and at flows in the order of mm/s the flow is well in the region of laminar flow. The size of the phantom is another thing that had to be adapted to the different set ups. In figure 5.1, a schematic image of the tissue phantom is given. The phantom produced was made to

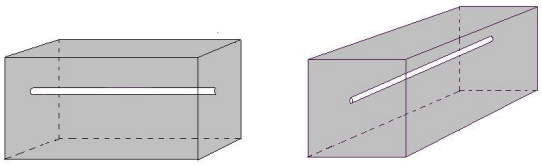

Figure 5.1: In the figure above a schematic image of a tissue phantom is presented.

mimic tissue at the wavelength 1300 nm, and has a hole with diameter $d = 300$ μm that lies approximately 150 μm below the surface. The length of the tube in the phantom is 2 cm and in the device for attatching the hoses the holes

are gradually getting bigger. In figure 5.2 the phantom is shown with a hose attatched on one side.

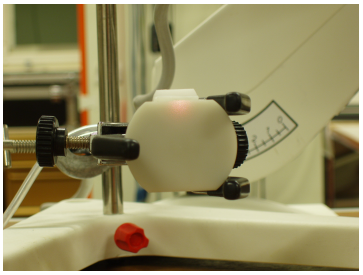

Figure 5.2: In the figure above a picture of the phantom is shown.

5.3 Making the tissue phantoms

When making the phantoms, epoxy resin, hardener, ink and TiO_2 were used. Special care had to be taken to follow preparation instructions for epoxy in order to avoid helth problems. The ink was used as an absorber while the TiO_2 was used as a scatterer. Since the two systems, DOCT and LDPI, are active at different wavelengths, 1300 nm and 633 nm respectively, the phantoms had to have optical properties matching those of skin for both 1300 nm and 633 nm, see table 5.1. It was possible to use the same phantoms for both systems, since the optical properties for tissue at 1300 nm and 633 nm did not differ more than a factor two. Phantoms for each of the systems were manufactured by varying the amount of ink and TiO_2. To make sure that the right amount of scatterer were added, Mie calculations were performed, and the result was compared to the known optical properties of tissue at the wavelength at issue. The amount of absorber to add was also calculated. The calculations were performed with help of a program called *epoxy_recipe* written by David Levitz.
In order to give the fluid in the tubes optical properties similar to human blood different concentrations of Intralipid were used.
The phantoms were made by first mixing the precalculated amounts of hardener, ink and TiO_2, and then put the mix in an ultra sound bath for two hours, whereafter the hardener solution was mixed with the epoxy resin and slowly stirred for one hour in order to make the solution more homogenous. To harden properly the phantoms first had to be left in room temperature for 12-16 hours and then they had to be put in an oven at $55 - 60°C$ for 24 hours. If the phantoms were left to harden only in room temperature they turned out to be fragile, and not at all easy to process.
In order to get the desired shape of the phantom it was first grinded to appropriate size whereafter a small hole were drilled through the phanotm, close to the surface. The diameter of the hole was 300 μm, and the distance between the hole and the surface was approximately 150 μm.
The small diameter of the hole made it difficult to drill long distances, and therefore three pieces were glued together. The middle part consisted of the phantom with the small hole and in the end parts hose attatching devices, with

larger holes in, were glued on with heat activated glue. Through the hose fluid could be led into the small hole, through the phantom and then out into the hose again. A schematic image of the tissue phantom can be seen in figure 5.1.

Optical properties $[mm^{-1}]$	*1300 nm*	*633 nm*
Absorption coefficient, μ_a	0.2 ± 0.01	0.21 ± 0.05
Scattering coefficient, μ_s	11 ± 2	22.4 ± 3

Table 5.1: In the table above the optical propertis of tissue at the wavelengths 1300 nm and 633 nm are presented.

Chapter 6

Computer simulations

When measuring flow with DOCT a ring pattern due to a folding phenomena occurs in the generated images, see figure 6.1. These rings indicate the size of the Doppler frequency shift, and in that way they provide information on the velocity of the moving scatterers.

As mentioned in section 3.2 it is the autocorrelation function, R, that gives rise

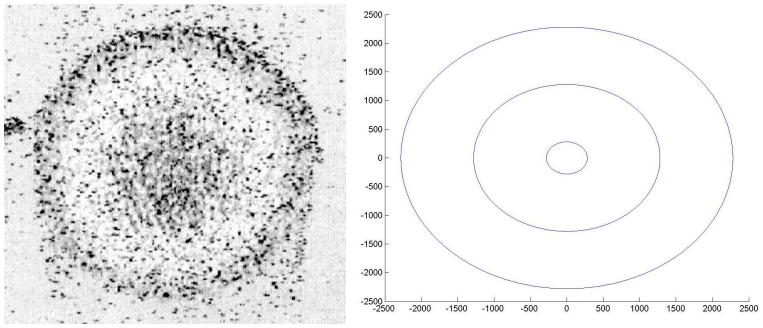

Figure 6.1: In this figure the ring pattern generated when measuring the flow velocity is illustrated as well as the ring pattern generated when simulating flow velocities exceeding the monotonic range.

to the foalding phenomena, which in turn generates rings in the OCT image.
A program that simulated flow measurements with a Doppler-OCT system and then generated the number of rings that would have appeared in a real Doppler-OCT image was constructed.
This was done as a preparation for the real measurements with the Doppler OCT system, and provided information on whether to expect rings or not at the velocities that were going to be used during the measurements.
Figure 6.1 is an exmple of an image with simulated flow exceeding the monotonic range of the system.

The full Matlab code can be seen in appendix B.

Chapter 7

Measurements on tissue phantom

As a preparation for measurments on human skin, measurements on an epoxy based tissue phantom containing a small tube with laminar flow were performed. In this section those measurements will be presented.
All measurements were performed with both the Laser Doppler Perfusion Imaging system and the Doppler Optical Coherence Tomography system.
Since the systems are slightly different, the set ups had to be varied. Hence the optical arrangements will also be described briefly below.

7.1 The set ups

During measurements the tissue phantom was mounted in a holder in order to prevent movement artifacts generated by, for example the pump.
Even though effort was made to make the set ups, and other conditions, as similar as possible for the two systems, some small adjustments had to be made to meet the specific requirements of each system.
In figures 7.1 and 7.2 the probe and phantom set ups are shown for the DOCT and the LDPI system, respectively.
As can be seen in figure 7.1 the phantom is not mounted with the surface par-

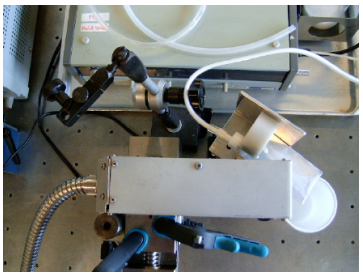

Figure 7.1: In this figure the DOCT set up for Intralipid measurements is illustrated.

allell to the probe, but at an angle. That is due to the need of a Doppler-angle

when using the DOCT system.
If the surface of the phantom were parallell to the probe, no Doppler shift would be detected, since the light would have normal incidence on the flow and hence be perpendicular to the moving scatterers. It is important that the laser light is focused inside the tube, so to enable small adjustments of the set up the phantom was mounted on a movable holder close to the probe.
When performing measurements with the LDPI system, on the other hand, the phantom was mounted with the surface parallell to the probe, as can be seen in figure 7.2. The distance between the probe and the phantom surface was 20 cm.
As mentioned earlier in chapters 3 and 4, the DOCT and LDPI systems gen-

Figure 7.2: In this figure the LDPI set up for Intralipid measurements is illustrated.

erates images showing different cross-sections of the sample. The LDPI system generates images of the surface with the flow showing as a line, either vertically or horisontally, see figure 7.3, and since all information about the flow will be contained in one line the phantom was rotated 90° after the measurements and new images were recorded in the same way as earlier, in order to avoid system generated artefacts.
The images generated by the DOCT system, on the other hand, shows a cross-section of the tissue and therefore the flow will show as a circle in the images, see figures 7.4 and 7.5, and there will be no need for rotating the phantom. When

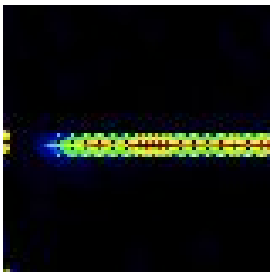

Figure 7.3: In this figure an image generated by the LDPI system is shown. The flow through the phantom is represented by the colored line through the image. The black area surrounding the line represents the phantom. The more perfusion in the sample the more red in the color scale.

performing measurements with the DOCT system several different images are generated, see figures 7.4 and 7.5, and they all contain valuable information.

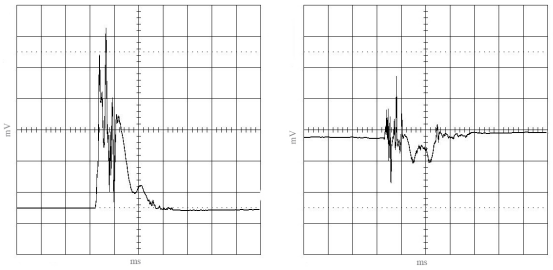

Figure 7.4: In the figures above images generated by the DOCT system are shown. The left hand image show the averaged envelope signal, and the right hand image show the averaged frequency signal where the parabolic shape in the middle represents the flow. The noisy part before and after the parabolic shape is probably due to the tissue phantom. In this image the parabolic shape has got a dip in it, due to the velocity of the moving scatterers in the phantom. The velocity in this image is higher than the DOCT system can resolve, hence the folding phenomena in the flow profile.

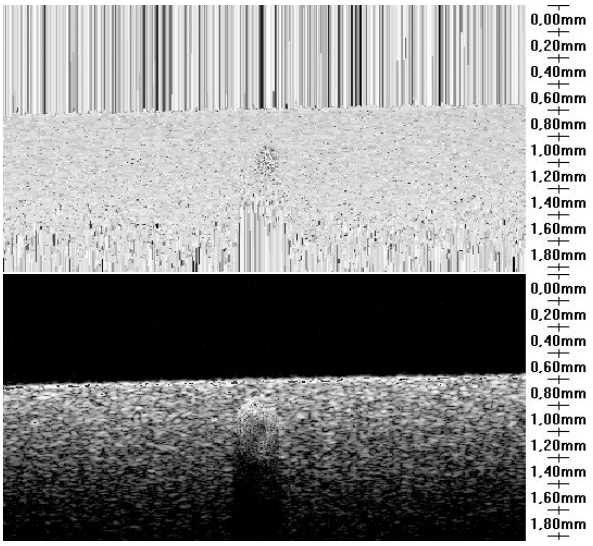

Figure 7.5: In the figures above images generated by the DOCT system are shown. The upper image show the OCT image obtained from the frequency signal. The circle in the middle is the hole through the phantom and the surrounding grey area is the epoxy phantom. The lower image show the OCT image obtained from the envelope signal. The scale on the right hand side of the images show the distance from the probe.

The averaged frequency signal provides information on the velocity of the scatterers. The parabolic shape in the right hand image in figure 7.4 gives the flow profile. Depending on the direction of the flow, the parabolic shape will point upwards or downwards, and if the flow is higher than the system can detect a folding phenomena will occur causing a dip, or peak, in the flow profile.
In the right hand side image in figure 7.4 there are fluctuations in the signal

before and after the flow profile, probably caused by the light interacting with the phantom before it reaches the flow.
Those fluctuations does not disappear if the fluid in the tube is changed, but they disappear when Intralipid is lead through a glas tube.
The averaged envelope signal shows the damping of the signal as it passes through the phantom and the fluid in the tube. The damping differs depending on the properties of the fluid in the tube.
In figure 7.5 the OCT images generated by the DOCT system during measurements on a tissue phantom is shown. The lower image is generated by the envelope signal and is hence and ordinary OCT image showing the cross-section of the phantom, while the upper image is generated by the frequency signal and hence provides information on the frequency shifts and in that way the flow.

The pump used during the measurements with the DOCT system is not the same pump used during the measurements with the LDPI system. Careful calibrations were therefore performed in order to have the same flow velocity in the phantom during all measurements.

7.2 Measurements

In order to test the resolution, linearity and the systems ability to resolve various flows, see table (7.1), in a tissue phantom ten different flow velocities were measured with both the systems.
Intralipid, in three different concentrations, and water was used as fluid in the phantom, and reference measurements were performed with air.

Velocity in ml/s	*Corresponding velocity in mm/s, in a tube with* $d = 0.3mm$
0.004172	59.0
0.003131	44.3
0.002117	30.0
0.00184	26.6
0.00132	18.7
0.000869	12.0
0.000637	9.0
0.000417	5.9
0.000320	4.5
0.000215	3.0

Table 7.1: In the table above the velocity in mm/s of the flow in a tube with a diameter of 300 μm is given for ten different flow velocities in ml/s.

The flow velocities in mm/s were calculated with the following equation:

$$v_{mm/s} = \frac{v_{mm^3/s}}{A_{cross}} \tag{7.1}$$

where $v_{mm/s}$ is the velocity in mm/s, $v_{mm^3/s}$ is the flow in mm^3/s, i.e. in $0.001ml/s$, and A_{cross} is the cross-sectional area of the tube, i.e. $A_{cross} = \pi r^2$

where r is the radius of the tube.
Since two different pumpes were used, one in the DOCT set up and one in the LDPI set up, both pumps had to be calibrated and the pump settings corresponding to the flow velocities had to be determined.
This was done by measuring the time it took for the pumps to empty a certain amount of fluid. The corresponding flow velocities could be determined by doing this at all the different pump settings.
Since the measurements were first performed with the DOCT system, the pump settings on the pump used during the LDPI measurements had to be adapted to the velocities given by the pump in the DOCT set up.

Laminar flows In order to make sure that the flow in the phantom was actually laminar the following calculation was performed for the different flow velocities:

$$Re = \frac{v_{mm/s} \cdot r}{\nu} \tag{7.2}$$

Where $v_{mm/s}$ is the flow velocity in the tube, r is the radius of the tube and ν is the kinematic viscosity of the fluid.
The flow is known to be laminar as long as Reynolds number, Re, is smaller than 1000, which were the case for all the measurements performed with the two systems.
There are many varieties of the formula for calculating Reynolds number, and different formuals have different boundary values for the laminarity of the flow.
The laminarity of the flow is important since a laminar flow in a circular tube gives rise to a parabolic velocity profile, see equation 7.3, [20].

$$v_{mm/s}(r) = v_c\left[1 - \left(\frac{r}{d/2}\right)^2\right] \tag{7.3}$$

where $v_{mm/s}(r)$ is the velocity at radial position r, v_c is the central peak velocity and d is the diameter if the tube.
A parabolic flow profile is shown in figure 7.6.

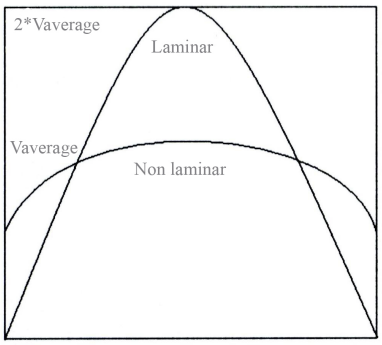

Figure 7.6: In this figure the parabolic flow profile of a laminar flow in a circular tube is illustrated. The higher curve shows a laminar flow while the lower curve shows a non liaminar flow.

7.2.1 Intralipid measurements

Intralipid was used as the fluid in the tube since it has a high scattering coefficient, something that is necessary in order to get some Doppler shifted backscattered light to the detectors.
By varying the concentration of the Intralipid solutions, the amount of backscattered light will also vary and the concentration dependence can be extracted from the data.
Therefore three different concentrations of Intralipid solutions were used for the measurements.
Since the fluid in the tube was supposed to mimic blood it would probably have been better if water containing small microspheres, for the scattering effects, and ink, for the absorption, were used. However, taking into account that the ink could color the phantom and the microspheres could clog the tube, Intralipid was choosen as the fluid.

Intralipid solution 3% A solution with water and 3% Intralipid was used as the fluid in the tube, and therefore the pump was filled with this solution.
During the measurements the phantom was kept fixed and the velocity in the tube was changed by changing the pump-velocity. After the pump-velocity was changed, the pump was left to stabilize before the measurements, in order to avoid artefacts due to velocity changes in the pump.
In figure 7.7 the perfusion as a function of the flow velocity in the phantom with the 3% Intralipid solution, measured with the LDPI system, is shown.
As can be seen the perfusion response is not linear and this is due to the range

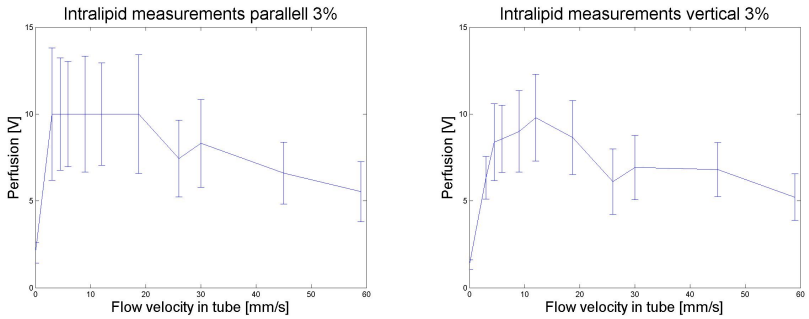

Figure 7.7: In this figure the perfusion, i.e. the measured intensity, as a function of the velocity in the phantom for the LDPI system is shown for a 3% Intralipid solution, i.e. the measured intensity is plotted as a function of the actual velocity in the tube.

of velocities choosen for the measurements.
The LDPI system is adapted for measuring lower flows than the DOCT system, and hence the range that fits the DOCT system well will be too high for the LDPI system, resluting in non-linearity.
The LDPI system is supposed to be linear up to a velocity of 3 mm/s and that is the lowest velocity in this measurement series, besides the zero velocity measurement, and hence the curve showing the perfusion as a function of the velocity will not show any linearity.

The maximum perfusion to be measured with the LDPI system is 10 V and therefore irregularities can appear when the perfusion gets higher.

The same measurements were performed with the DOCT system and the result is shown in figure 7.8. The DOCT system is linear up until 10 mm/s

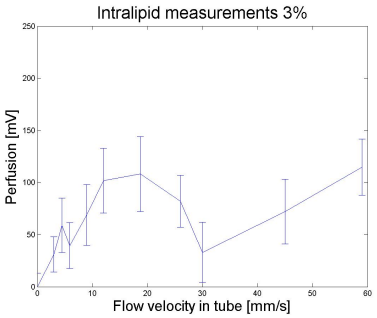

Figure 7.8: In this figure the measured intensity as a function of the flow velocity in the phantom for the DOCT system is shown for a 3% Intralipid solution, i.e. the measured intensity is plotted as a function of the actual velocity in the tube.

and then it shows nonlinear behaviour. The shape of the curves obtained with the DOCT system resemblance the shape of the curves obtained by the LDPI system.

Intralipid solution 2% The same procedure as for the measurements with the 3% Intralipid solution was followed with the 2% Intralipid solution.
All the flow velocities were imaged, and in figures 7.9 and 7.10 the measured intensity as a function of the flow velocity in the phantom for a 2% Intralipid solution is shown for both the LDPI and the DOCT systems. The curves

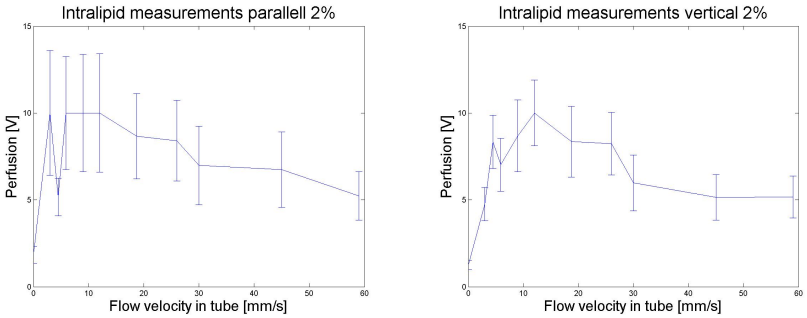

Figure 7.9: In this figure the perfusion, i.e. the measured intensity, as a function of the velocity in the phantom for the LDPI system is shown for a 2% Intralipid solution, i.e. the measured intensity is plotted as a function of the actual velocity in the tube.

in figures 7.9 and 7.10 show the same behavoiur for the 2% Intralipid solution as for the 3% solution with the difference that the measured intensity in the images generated by the LDPI system seems to drop with decreasing Intralipid concentration. This is probably due to the decrease in scatterers in the fluid

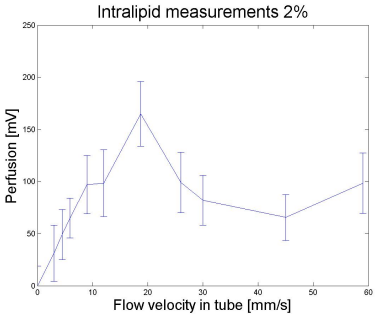

Figure 7.10: In this figure the the measured intensity as a function of the flow velocity in the phantom for the DOCT system is shown for a 2% Intralipid solution, i.e. the measured intensity is plotted as a function of the actual velocity in the tube.

which in turn decreases the amount of backscattered, Doppler-shifted, light.
With a much higher concentration of Intralipid the increased amount of scatterers would most likely decrease the amount of backscattered light, since the number of multiple scattering events would increase.
The curves generated by the DOCT system also show the same behaviour for the 2% and 3% Intralipid solution, but the intensity seem to get higher with lower intralipid concentration.
This might be a result of the amount of scatterers in the solutions. The 3% Intralipid solution contains more scatterers than the 2% solution and because of the large amount of scatterers in the 3% solution, more multiple scattering events might occur decreasing the amount of backscattered light, lowering the measured intensity.

Intralipid solution 1% The same procedure as for the measurements with the 3% and 2% Intralipid solutions was followed with the 1% solution.
Also here the measurements were performed with both the LDPI and the DOCT systems.
In figures 7.11 and 7.12 the measured intensity as a function of the flow velocity in the phantom for a 1% Intralipid solution is shown for both the LDPI and the DOCT systems. Compared to the curves obtained with the 2% and 3% Intralipid solutions the curve for the 1% solution is even lower in intensity for the LDPI system, but is still showing the same curvature and pattern.
By further decreasing the number of scatterers compared to the 2% solution the intensity dropped further and the connection between the number of scatterers and the resulting intensity could be confirmed.
The curve obtained with the DOCT system and the 1% Intralipid solution still showed recemblance with the curves for the 2% and 3% Intralipid solutions, but the measured intensity was higher for the 1% solution. This might be due to decreased multiple scattering. By lowering the concentration of scatterers even further the intensity will probably decrease due to lack of scatterers.

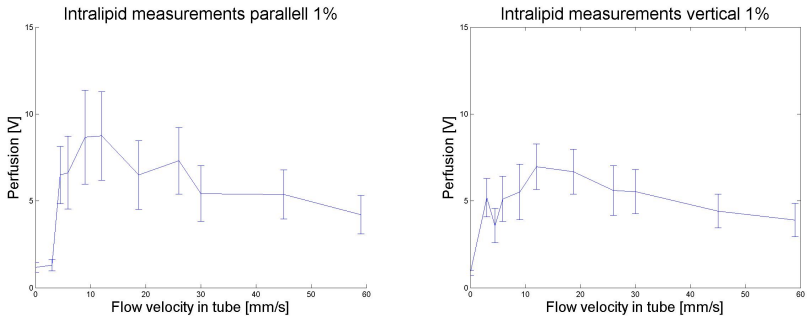

Figure 7.11: In this figure the perfusion, i.e. the measured intensity, as a function of the velocity in the phantom for the LDPI system is shown for a 1% Intralipid solution, i.e. the measured intensity is plotted as a function of the actual velocity in the tube.

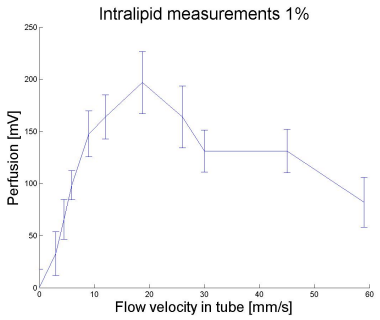

Figure 7.12: In this figure the the measured intensity as a function of the flow velocity in the phantom for the DOCT system is shown for a 1% Intralipid solution, i.e. the measured intensity is plotted as a function of the actual velocity in the tube.

7.2.2 Water measurements

Since water has a much lower scattering coefficient than Intralipid, measurement with water was performed with the LDPI system to further demonstrate the signal dependece on the scattering coefficient.
The same procedure as for the Intralipid measurements were followed when doing the water measurements.
Before the water measurements the phantom was cleaned in order to get rid of all the Intralipid solutions.

In figure 7.13 the measured intensity as a function of the flow velocity in the phantom is shown when water was used as the fluid in the phantom and LDPI was the system being used. As can be seen the measured intensity is very low, as expected, but the behaviour of the curves still recemblance the curves obtained with the Intralipid solutions as the fluid. This is probably due to some rests of Intralipid in the phantom scattering the light.

Measurements with water were also performed with the DOCT system in order to investigate the cause of the noisy behaviour of the averaged frequency

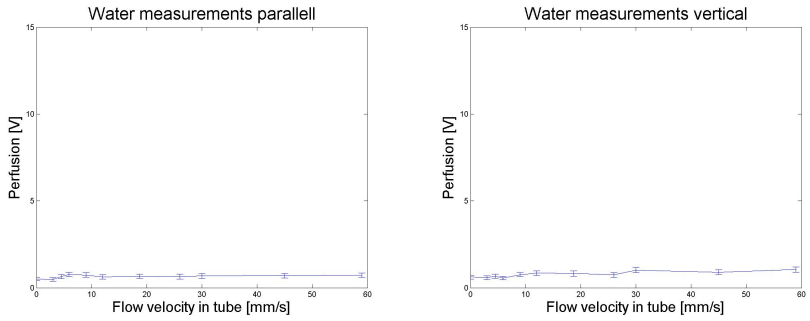

Figure 7.13: In this figure the the measured intensity as a function of the flow velocity in the phantom for the LDPI system is shown with water as the fluid, i.e. the measured intensity is plotted as a function of the actual velocity in the tube.

signal slightly before and after the flow profile. As can be seen in figure 7.14 changing the fluid from Intralipid to water does not change the behaviour of the signal, which indicates that it probably is due to the structure of the tissue phantom itself. In the averaged frequency signal there is no parabolic shape, and hence no flow could be detected.

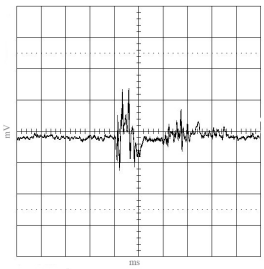

Figure 7.14: In this figure the averaged frequency profile of the water measurements is shown. As can be seen in the image the noisy part before and after the flow profile does not change when water is used as the fluid.

7.2.3 Air measurements

Even measurements with air in the tube instead of water or Intralipid were performed. Those measurements were only performed to show that no Doppler shift could be recorded unless there were larger, moving, scattering particles in the tube.
The averaged frequency signal showing the flow profile for the air masurement with the Doppler OCT system is shown in figure 7.15. The profile shows the same behaviour as for water and Intralipid measurements with low, or no flow, i.e. there is no parabolic shape. The effects due to the tissue pantom structure is still clearly visible. The images generated by the LDPI system did not show any signs of perfusion when air was present in the tube, see figure 7.16.
The color scale in the LDPI system is changed for the air measurements, and

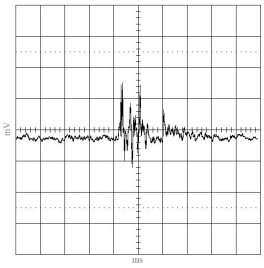

Figure 7.15: In this figure the averaged frequency profile of the air measurements is shown. As can be seen in the image the noisy part before and after the flow profile does not change when air is used as the fluid.

the range is very small. Although the air is flowing in the tube the system can not resolve it, hence the whole image is colored.

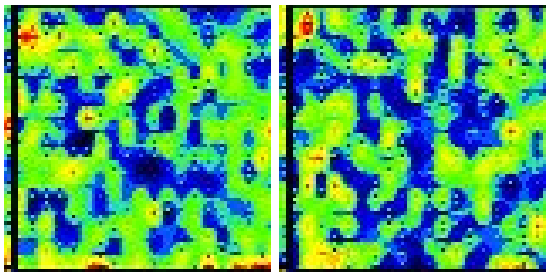

Figure 7.16: In this figure images generated by the LDPI system when the phantom is filled with air is shown. The left image is generated with the hole as a horisontal line in the scan and the right image is generated with the hole as a vertical line in the scan.

7.3 System comparison

Even though the two systems, DOCT and LDPI, generate images with different cross-sections the information obtained from the images have much in common. Both systems show linearity up to a certain velocity limit whereafter the linear behavior stop. The LDPI system is adapted to fit lower flows, hence the limit for linearity in the flow measurements is lower than for the DOCT system.
When decreasing the concentration of scatterers the intensity measured with the LDPI system decreases, while the intensity measured with the DOCT system increases.
The LDPI system is frequently used in clinics for perfusion measurements and hence adjusted to measure blood perfusion in tissue. Since blood is highly scattering and absorbing, this can explain why the intensity drop for the LDPI system when the scatterer concentration decrease.
The DOCT system has not been used on blood samples yet, and the concentrations of Intralipid that have been used have been low in comparison to blood.

During measurements on the tissue phantom the DOCT system has generated two-dimensional images, but it is also possible to generate three-dimensional images with this system.
The three-dimensional images takes longer time to record, and therefore the two-dimensional images were used during the above mentioned measurements.

Apart from the obvious differences in the images generated, the systems provided similar information regarding the flow in the phantom.
An advantage with the DOCT system is that it is possible to determine at what depth the flow is located, while the LDPI system only provide information on the average blood perfusion in a sample.
The main advantage with the LDPI system is the set up and analysis programs. Since the LDPI system is adapted for meaurements in clinics, the scanner head is easy to adjust and the programs generating the images and data is very user-friendly.
When it comes to usability the DOCT system is far behind the LDPI system. The DOCT probe is rather big and not easy to handle and it needs to be fixed during measurements. The laser beam also needs to be focused inside the flow in the sample in order to get a reliable signal.
The adjustments needed to get a good signal from the DOCT system takes a lot of time and requires an exact knowledge of the location of the flow, something that is not always easy.

Chapter 8

Measurements on skin

The skin measurements in this study were performed on the forearm. The volunteer rested for 20 minutes before the measurements, that were performed in a room with controlled temperature (25°)C.
Before and during the measuremenst the arm was fixed in a relaxed position and the area to be measured on was marked in order to know where to apply the stimulation.
Blood perfusion measurements on the forearm skin has been done before with LDPI [56][65].

8.1 Stimuli description

By gently scratching the skin on the forearms an increase in blood flow can be achieved. This increase will start a few seconds after the scratch and last for several minutes. This stimulation was used in this study since it is fairly easy, and reproducable.
In figure (8.1) the mark after a scratch is illustrated. Along the line of the scratch there will be a red ridge, and surrounding the ridge a white, slightly swollen area. Outside the white area will be a larger red area. In all these areas there will be an increased blood perfusion.

Figure 8.1: In this figure a scratch mark on the forearm is shown. Red marks caused by a pen in order to show how to position the probe is also visible.

8.2 The set ups

The set ups used for skin measurements are shown in figures 8.2 and 8.3. During the measurements the subject was sitting still, and the temperature in the room was kept constant, not to affect the blood perfusion.

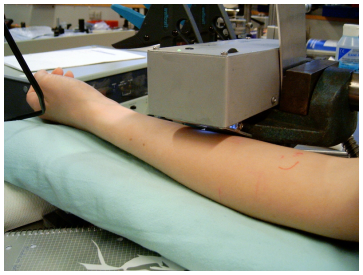

Figure 8.2: In this figure the DOCT set up used during the skin measurements is shown.

Figure 8.3: In this figure the LDPI set up used during the skin measurements is shown.

The skin measurements with the LDPI system were non contact measurements, at a distance of 20 cm between the surface of the skin and the detector. The measurements with the DOCT system were performed with as well as without contact. The contact mesurements were performed with a water based ultrasound gel between the skin and the detector in order to enhance the signal, while the non-contact measurements were performed at a short distance from the skin.

8.3 Measurements

The skin measurements were performed following a predefined protocol.
The first meaurement was performed before the stimulation was applied and then measurements were conducted every minute after the stimulation up until 15 minutes after the stimulation, according to table 8.1.

The number of measurements performed	*Measurement times in minutes after the stimulation*
1	Before stimulation
2	1
3	2
4	3
5	4
6	5
7	6
8	7
9	8
10	9
11	10
12	11
13	12
14	13
15	14
16	15

Table 8.1: In the table above the times for the skin measurements are presented.

8.3.1 DOCT

The skin measurements with the DOCT system were performed both as contact and as non-contact measurement.
The signal can be improved with use of a water based ultrasound gel between the probe and the skin. This signal improvement enables imaging of deeper lying structures in the tissue since the returning signal will be stronger and in that way not drowned in noise.

Non-contact measurements In figures 8.4 - 8.6 the penetration depth as a function of time after the stimulation is shown. No direct perfusion signal could be seen, so the perfusion was instead evaluated in a very indirect way.
Right after the stimulation a decrease in penetration depth can be seen, indicating an increase in blood perfusion, and then the penetration depth slowly increases again, indicating a decrease in blood perfusion.
When the amount of blood in the tissue sample increase, the optical properties of that sample change, yielding a change in penetration depth of the laser. In the wavelength region around 1300 nm an increase in blood in the tissue sample will increase the scattering coefficient and in that way decrease the penetration depth.
So, by detecting the change in penetration depth, information on changes in blood perfusion can be extracted.
Three different non-contact measurements were performed and the results can be seen in figures 8.4-8.6.

The results from the non-contact meaurements show that the depth from which a signal can be retrieved in the tissue, changes after the applied stimulation.

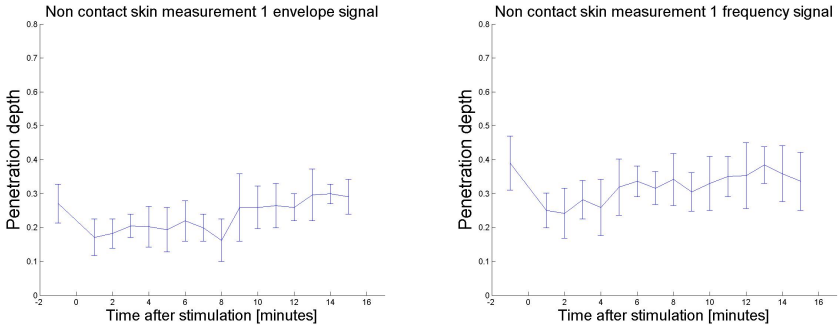

Figure 8.4: In this figure the penetration depth of the signal as a function of time after the stimulation for the first non-contact measurement is shown. The left hand image shows the time dependent penetration depth for the envelope signal and the right hand image shows the time dependent penetration depth for the frequency signal.

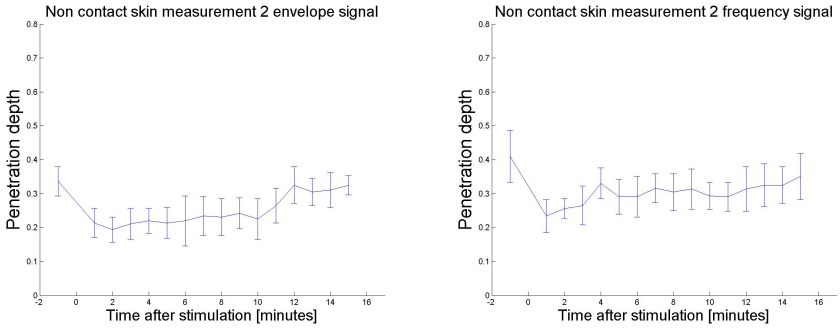

Figure 8.5: In this figure the penetration depth of the signal as a function of time after the stimulation for the second non-contact measurement is shown. The left hand image shows the time dependent penetration depth for the envelope signal and the right hand image shows the time dependent penetration depth for the frequency signal.

For a few minutes after the stimulation the penetration depth decrease, indicating an increase in blood flow in the tissue, and after a few minutes the penetration depth starts to increase again and then it returnes to the value it had before the stimulation.
This behaviour corresponds well to the known behaviour of the blood perfusion in tissue after a superficial stimulation.
Although changes in blood perfusion could be detected by monitoring the behaviour of the penetration depth over time, no other structures in the OCT images indicated vessels or areas with locally increased perfusion. This is probably due to a few factors such as the shallow penetration depth, around 1 millimeter, the range of flows that the system is able to detect and the geometrical resolution of the system.

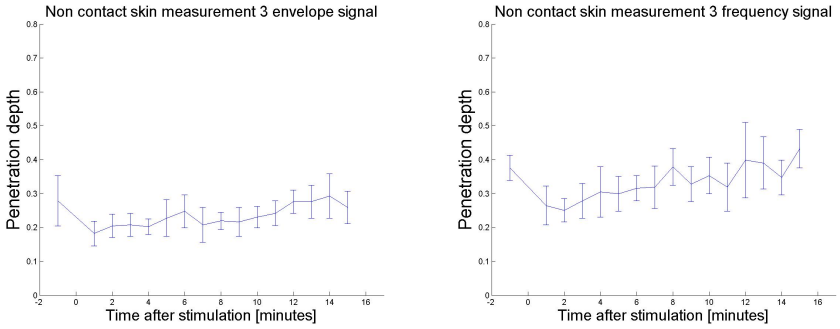

Figure 8.6: In this figure the penetration depth of the signal as a function of time after the stimulation for the third non-contact measurement is shown. The left hand image shows the time dependent penetration depth for the envelope signal and the right hand image shows the time dependent penetration depth for the frequency signal.

Contact measurements Three different contact measurements were also conducted with the DOCT system.
In figures 8.7-8.9 the penetration depth as a function of time after the stimulation is shown. Right after the stimulation a decrease in penetration depth can be seen, indicating an increase in blood perfusion, and then the penetration depth slowly increases again, indicating a decrease in blood perfusion. The re-

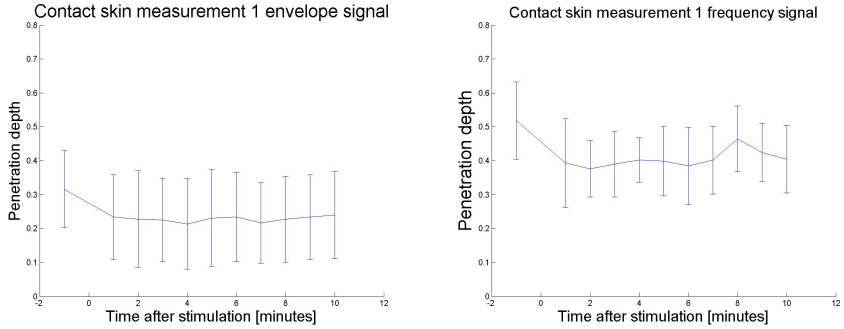

Figure 8.7: In this figure the penetration depth of the signal as a function of time after the stimulation for the first contact measurement is shown. The left hand image shows the time dependent penetration depth for the envelope signal and the right hand image shows the time dependent penetration depth for the frequency signal.

sults from the contact measurements also show a decrease in penetration depth after the stimulation and then a gradual increase in penetration depth again.
The main difference between the images generated during the non-contact and the contact measurements is the initial penetration depth. The measurements performed with the water based gel between the probe and the detector showed deeper lying structures than the measurements performed without the gel. The water based gel that was used as a layer between the probe and the skin de-

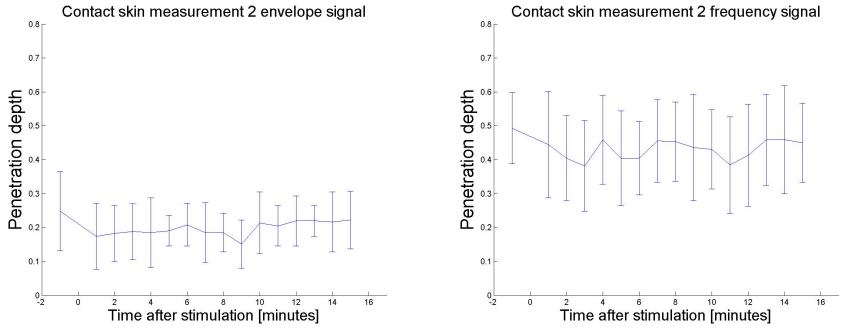

Figure 8.8: In this figure the penetration depth of the signal as a function of time after the stimulation for the second contact measurement is shown. The left hand image shows the time dependent penetration depth for the envelope signal and the right hand image shows the time dependent penetration depth for the frequency signal.

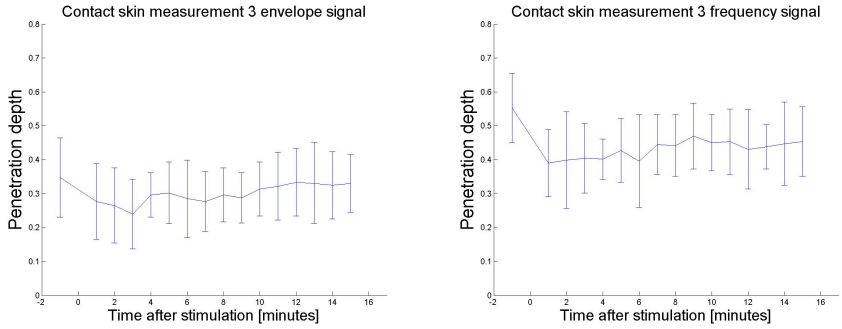

Figure 8.9: In this figure the penetration depth of the signal as a function of time after the stimulation for the third non-contact measurement is shown. The left hand image shows the time dependent penetration depth for the envelope signal and the right hand image shows the time dependent penetration depth for the frequency signal.

creased the loss of signal due to reflections on the skin surface and hence increased the signal to noise ratio and in that way also increased the depth at from which a signal could be obtained.
Even though the penetration depth was larger with the contact measurments no vessel structures or areas with locally increased blood perfusion could be detected.
The decrease in penetration depth due to locally increased blood perfusion seemed to be a bit more pronounced in the non-contact measurements than in the contact measurements.

8.3.2 LDPI

In figure 8.10 the perfusion as a function of time after the stimulation is shown. Right after the stimulation an increase in blood perfusion can be seen, and then

the perfusion will slowly decrease with time. As can be seen in the figures the

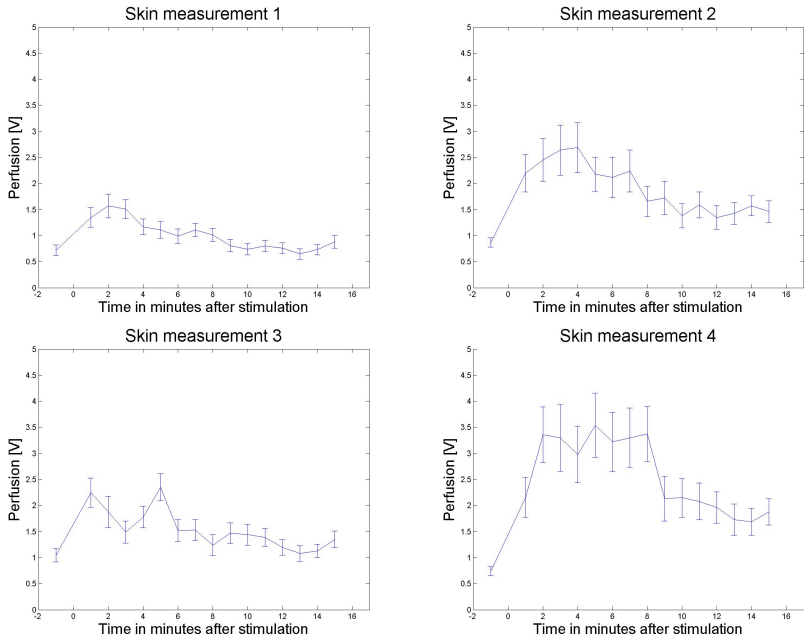

Figure 8.10: In this figure the perfusion as a function of time after stimulation is shown for four different stimulations. The measurements were performed with the LDPI system.

four perfusion curves all decrease after a few minutes, which indicates a decrease in blood perfusion in the tissue.
This behaviour is documented, and after stimulation the perfusion is supposed to increase after about 30 seconds and then it will start to decrease again after a few minutes and it has returned to normal again after approximately 15-20 minutes.
The images generated by the LDPI system did not only provide information on the time dependence of the blood perfusion but also on the size of the area around the scratch mark that were affected. The gradual decrease in blood perfusion with increasing distance to the mark was clearly visible in the images.

8.4 System comparison

During the skin measurements it was not possible to see any blood vessels or locate any flows with the DOCT system. This was probably due to the fact that the velocity of the blood flow in the tissue was lower than what the system could detect.
Despite that it was possible to indirectly see changes in blood perfusion in the tissue. This could be done by studying the depth of the returning signal, i.e. how deep down in the tissue it was possible to resolve something.
When the amount of blood change, the optical properties in the tissue change and that affects the penetration depth of the light. So, by measuring the pene-

tration depth in the generated images the change in blood flow could be monitored.

The LDPI system was very easy to handle when it was time for the skin measurements, and the images generated by the system showed where there were an increase in blood flow.
By plotting the perfusion as a function of time after the stimulation, conclusions on the time dependent perfusion could be drawn, and comparisons be made between the two systems.
Both the data from the LDPI system and the data from the DOCT system showed an increase in blood flow after the stimulation and then a gradually decreasing perfusion that returned to normal after a few minutes.

The main disadvantage with the DOCT system when it comes to skin measurements is the rapid decrease in signal when the distance between the sample and the probe increase. The probe had to be positioned as close to the tissue surface as possible, i.e. in the range of mm from the surface, and in order to get a decent signal a water based gel had to be applied on the skin.

During skin measurements like this the LDPI system was clearly to prefer, due to its flexibility and image generation.
The images obtained by the LDPI system provided information on how large the affected area was and and in what parts of the area the perfusion was high.
The change in structure in the images obtained by the DOCT system indicated an increase in blood flow, but nothing was clearly visible. Not even larger vessels could be detected.
By increasing the penetration depth and by adapting the system to fit lower flows it could be possible to detect vessels and other structures in tissue.

Chapter 9

Conclusions

As of today, of the two systems studied the LDPI system is capable of resolving lower flows than the DOCT system, and therefore more suitable for flow measurements. However, when the DOCT system can resolve lower flows it will be valuable, since it also generates three dimensional images of the internal structure. This will enable monitoring of the vessel structure and flow.
The DOCT system can resolve flows down to 3 mm/s, which is higher than the flow in the superficially lying vessels in the skin. This in combination with the shallow penetration depth makes imaging of vessel structures and areas with local perfusion changes impossible. The depth at which structures can be resolved at the moment is between 0.3 - 0.8 mm below the tissue surface.
When it comes to calibration measurements on epoxy based tissue phantoms both the DOCT and the LDPI system provided similar information but the LDPI system was more user-friendly and had better developed programs for data analysis.
During skin measurements the LDPI system provided information, not only on the amount of perfusion in the tissue, but also on the size of the area affected by the stimulation. The images generated by the DOCT system, on the other hand, did not show any direct signs of vessel structures or locally increased blood perfusion. It was, however, possible to detect changes in blood perfusion by monitoring the time dependent variation in penetration depth after stimulation.
The information gained from the two systems during the skin measurements showed the same time dependent perfusion changes after stimulation.

Chapter 10

Future tasks

As of today the Doppler Optical Coherence Tomography system at Risø can resolve flows above 3 mm/s, and in order to measure blood flows in the capillaries in the skin, new solutions that enables the system to resolve lower flows are necessary. That in combination with simultaneous measurements of Doppler angle and Doppler shift would increase the usability of the system alot.
A new probe on an adjustable arm, in combination with a low power laser beam in the visible region for guidance would also considerably increase the usability of the system and make it more attractive for use in the clinic.
The possibility of making three-dimensional tomographic images of the vessel structure and flow is another interesting application for this type of system.
Once lower flows can be measured, new skin measurements needs to be performed before the system can be used for measurements in connection with PDT treatment, as was the initial aim.

Acknowledgements

I would like to thank the following persons, whose assistance greatly contributed to this project,
my supervisor in Lund professor Stefan Andersson-Engels for introducing me to the subject and encouraging me when things did not go as planned.
Senior Scientist Peter E Andersen, Scientist Lars Thrane and Reasearch Technician Finn Pedersen at Risø for all the invaluable help with the Doppler-OCT system.
The medicine group at the Atomic physics department in Lund.
The OCT group at Risø.
Professor Karin Wårdell at the Department of Biomedical Engineering in Linköping, and the rest of the group for making me feel welcome during my visit.
Lana Bosanac for the company and nice discussions during the long hours in the lab, and all the other help during this project. Thank you!
Anna for the lunch company and all the fun, and encouraging, discussions.
My family for the support.
Finally, I would like to thank those not mentioned by name, but who in one way or another have contributed to this project.

Bibliography

[1] Welch A. J., van Gemert M. J. C. *Optical-thermal response of laser-irradiated tissue* pp 19-20, Plenum Press, New York, 1995

[2] Vo-Dinh T. *Biomedical Photonics Handbook* Chapter 15, Laser Doppler Perfusion Monitoring and Imaging Taylor & Francis Group (March 26, 2003)

[3] Jönsson G. *Atomfysikens Grunder, del I* pp 109-110, Third Edition, Tech Support, Lund, Sweden, 1998

[4] Welch A. J., van Gemert M. J. C. *Optical-thermal response of laser-irradiated tissue* pp 842, Plenum Press, New York, 1995

[5] Henyey L. C., Greenstein J. L. *Diffuse radiation in the galaxy.* Astrofys. J., V 93 pp 70-83, (1941)

[6] Welch A. J., van Gemert M. J. C. *Optical-thermal response of laser-irradiated tissue* pp 38, Plenum Press, New York, 1995

[7] *Medical optics web page* http://kurslab-atom.fysik.lth.se/FED4Medopt/ (2005-08-15)

[8] Welch A. J., van Gemert M. J. C. *Optical-thermal response of laser-irradiated tissue* pp 317, Plenum Press, New York, 1995

[9] Svanberg S. *Atomic and Molecular Spectroscopy* pp 65, Fourth Edition, Springer-Verlag, Berlin Heidelberg, Germany, 2004

[10] Welch A. J., van Gemert M. J. C. *Optical-thermal response of laser-irradiated tissue* pp 21-23, Plenum Press, New York, 1995

[11] Welch A. J., van Gemert M. J. C. *Optical-thermal response of laser-irradiated tissue* pp 73-74, Plenum Press, New York, 1995

[12] Welch A. J., van Gemert M. J. C. *Optical-thermal response of laser-irradiated tissue* pp 73-99, Plenum Press, New York, 1995

[13] Wennberg A M., Lindholm L. E., Alpsten M., Larkö O. *Treatment of superficial basal cell carcinomas using topically applied delta-aminolaevulinic acid and a filtered xenon lamp.* Arch Dermatol Res 288: 561-564, (1996)

[14] Allison R. R., Downie G. H., Cuenca R., Hu X. H., Childs C. J. H., Sibata C. H. *Photosensitizers in clinical PDT.* Photodiagnosis and Photodynamic Therapy 1, 27-42, (2004)

[15] Soto Thompson M. *Intelligent metod hittar och botar cancer* http://www-atom.fysik.lth.se/afdocs/PopularDescriptions/IntelligentMetod.pdf (2005-04-04)

[16] Vogl T. J., Eichler K., Mack M. G., Zangos S., Herzog C., Thalhammer A., Engelmann K. *Interstitial photodynamic laser therapy in interventional oncology* Eur Radiol 14:1063 - 1073(2004)

[17] Pedrotti F. L., Pedrotti L. S. *Introduction to optics* Page 184, Second edition, Prentice Hall Inc, Upper Saddle River, New Jersey, 1996.

[18] Yazdanfar S., Kulkarni M. D., Izatt J. A. *High resolution Imaging of in vivo cardiac dynamics using color Doppler coherence tomography.* Optics express 1, 424 (1997)

[19] R. Thorup Nilsen *Digital behandling og opsamling af videosignaler i forbindelse med optisk coherence tomografi* BSc Thesis, Risø, March 2004

[20] Wu L. *Simultaneous measurement of flow velocity and Doppler angle by the use of Doppler optical coherence tomography.* Optics and Lasers in Engineering 42 (2004) 303-313

[21] Huang D., Swanson A. E., Lin C. P., Schuman J. S., Stinson W. G., Chang W., Hee M. R., Flotte T., Gregory K., Puliafito C. A., Fujimoto J. G. *Optical Coherence Tomography* Science 5035, 3-254, p1178-1181, 1991

[22] Zagzebski J. A. *Essentials of Ultrasound Physics* Chapter 3, C.V. Mosby; 1st edition 1996

[23] Chen L. J. *Optical coherence tomography (OCT) findings following photodynamic therapy (PDT) in ophthalmology* Biophotonics, 2004. APBP 2004. IEEE 63-64 (2004)

[24] Rollins A. M., Yazdanfar S., Izatt J. A. *In vivo human retinal blood flow imaging using color Doppler optical coherence tomography* Lasers and Electro-Optics, 1999. CLEO '99.Opt. Soc. America

[25] Barton J.K., Hariri L., Tumlinson A. *Combined optical coherence tomography and fluorescence spectroscopy for characterization of tissues* Lasers and Electro-Optics Society, vol. 1 pp 458 - 459, 2003. LEOS 2003.

[26] Pierce M. C., Strasswimmer J., Park B. H., Cense B., de Boer J. F. *Advances in Optical Coherence Tomography Imaging for Dermatology* J Invest Dermatol 123:458 - 463, 2004

[27] Piao D., Chen N. G., Zhu Q., Dutta N. K., Otis L. L. *Imaging of fluid flow velocities using Doppler optical coherence tomography: preliminary results.* Bioengineering Conference, 2001. Proceedings of the IEEE 27th Annual Northeast IEEE 2001, 55-56

[28] Schaefer A.W., Reynolds J.J., Marks D.L., Boppart S.A. *Real-time digital signal processing-based optical coherence tomography and Doppler optical coherence tomography* Biomedical Engineering, IEEE Transactions: 2004 V: 51 Nr: 1 pp: 186-190

[29] Shakov A. V., Terentjeva A. B., Kamensky V. A., Snopova L. B., Gelikonov V. M., Feldchtein F. I., Sergeev A. M. *Optical coherence tomography monitoring for laser surgery of laryngeal carcinoma* Journal of Surgical Oncology, 77, 253-258, 2001

[30] Bouma B. E., Tearney G. J. *Optical Coherence Tomography: Introduction* Handbook of Optical coherence tomography Chapter 1, Marcel Dekker Inc, New York 2002

[31] Pedrotti F. L., Pedrotti L. S. *Introduction to optics* Page 201-204, Second edition, Prentice Hall Inc, Upper Saddle River, New Jersey, 1996.

[32] Pettersson S. G., Andersson-Engels S. *Photonics and Optical Communication* pp OPI-48, Department of Physics LTH, 2004

[33] Svanberg S. *Atomic and Molecular Spectroscopy* pp 233, Fourth Edition, Springer-Verlag, Berlin Heidelberg, Germany, 2004

[34] Svelto O. *Principles of Lasers* page 152, Plenum press, New York, fourth edition, 1998

[35] Zagzebski J. A. *Essentials of Ultrasound Physics* Chapter 5 - 6, C.V. Mosby; 1st edition 1996

[36] Westphal V. *Real-time microstructural and functional imaging and image processing in optical coherence tomography* Dissertation thesis, Universität Göttingen, January 2002.

[37] Rollins A. M., Kulkarni M. D., Yazdanfar S., Ungarunyawee R., Izatt J. A. *In Vivo Video Rate Optical Coherence Tomography* Optics Express 3 219-229 (1998)

[38] Angelsen B. A. *Instantaneous Frequency, Mean Frequency, and Variance of Mean Frequency Estimators for Ultrasonic Blood Velocity Doppler Signals.* IEEE Transactions in Biomedical Engineering 28 [11] 733-741, (1981)

[39] Kasai C., Namekawa K., Koyano A., Omoto R. *Real-Time Two-Dimensional Blood-Flow Imaging Using an Auto-Correlation Technique.* IEEE transactions on Sonics and Ultrasonics 32 [3] 458-464 (1985)

[40] Engelbrecht Larsen H., Thorup Nilsen R., Thrane L., Kristensen D. K., Pedersen F., Jørgensen t. M., Gualdino A., Andersen P. E. *Optical Doppler Coherence Tomography based on a Field Programmable Gate Array* Risø 2004

[41] Belo Gualdino A. *Doppler Otical Coherence Tomography* MSc thesis, Risø 2004

[42] Riva C., Ross B., Benedek G. B. *Laser Doppler measurements of blood flow in capillary tubes and retinal arteries* Invest Opthalmol 11(11):936-44 (1972)

[43] Stern M. D. *In vivo evaluation of microcirculation by coherent light scattering* Nature 254(5495):56-8 (1975)

[44] Essex T. J., Byrne P. O. *A laser Doppler scanner for imaging blood flow in skin* J Biomed Eng 13(3):189-94 (1991)

[45] Wårdell K., Jakobsson A., Nilsson G. E. *Laser Doppler perfusion imaging by dynamic light scattering* IEEE Trans Biomed Eng 40(4):309-16 (1993)

[46] Nilsson G. E., Tenland T., Öberg P. Å. *A new instrument for continous measurement of tissue blood flow by light beating spectroscopy* IEEE Trans Biomed Eng 27(1):12-9 (1980)

[47] Nilsson G. E., Salerud E. G., Strömberg N. O. T., Wårdell K. *Laser Doppler Pefusion Monitoring and Imaging* Biomedical photonics handbook, Vo-Dinh T. Editor. CRC Press, Boca Raton, Florida: 15:1-24

[48] Bonner R. F., Nossal R. *Principles of laser-Doppler flowmetry* Laser Doppler blood Flowmetry, Sheperd A. P, and Öberg P. Å. Editors. Kluwer Academic Publ., Boston:17-45 (1990)

[49] Bonner R. F., Nossal R. *Model for laser Doppler measurement of blod flow in tissue* Appl Opt 20(12):2097-107,(1981)

[50] Nilsson G. E., Jakobsson A., Wårdell K. *Tissue perfusion monitoring and imaging bu coherent light scattering* Proceedings of the SPIE-Bioptics: OPtics in Biomedicine and Environmental Sciences, Porto, Portugal, 17-15 March. 1524:90-109, (1991)

[51] Larsson M. *Influence of optical properties on laser Doppler flowmetry* Linköping studies in science and technology. Dissertation No. 914. Department of Biomedical Engineering, Linköping University, Linköping, Sweden, (2004)

[52] Serov A., Steenbergen W., de Mul F. *Prediction of the photodetector signal generated by Doppler-induced speckle fluctuations: theory and some validations* J Opt Soc Am 18(3):622-30 (2001)

[53] Karlsson D. *Movement artifact reduction in laser Doppler blood flowmetry* Dissertation No. 935, Linköping studies in Science and Technology

[54] Forrester A. T., Gudmundsen R. A., Johnson P. O. *Photoelectric mixing of incoherent light* Physical Rewiew 99(6):1691-1700 (1955)

[55] Lindén M. *High resolution laser Doppler imaging for microvascular blood flow measurements.* Dissertation thesis, Linköping University, Linköping Sweden, (1998)

[56] Fullerton A., Rode B., Serup J. *Studies of cutaneous blood flow of normal forearm skin and irritated forearm skin based on high-resolution laser Doppler perfusion imaging (HR-LDPI)* Skin Research and Technology 8: 32-40, Blackwell (2002).

[57] Cheong W. F., Prahl S. A., Welch A. J. *A review of the optical properties of biological tissues* IEEE Journal of Quantum Electronics, vol 26, no 12, p2166 - 2185, December 1990.

[58] Troy T. L., Thennadil S. N. *Optical properties of human skin in the near infrared wavelength range of 1000 to 2200 nm* Journal of Biomedical Optics 6(2), 167 - 176 (April 2001)

[59] Lualdi M., Colombo A., Farina B., Tomatis S., Marchesini R. *A Phantom With Tissue-Like Optical Properties in the Visible and Near Infrared for Use in Photomedicine* Lasers in Surgery and Medicine 28:237 - 243 (2001)

[60] Firbank M., Delpy D. T. *A design for a stable and reproducible phantom for use in near infra-red imaging and spectroscopy* Phys Med Biol 1993;38:847ś853

[61] Firbank M., Oda M., Delpy D. T. *An improved design for a stable and reproducible phantom material for use in nearinfrared spectroscopy and imaging* Phys Med Biol 1995; 40:955 - 961

[62] Flock S. T., Jacques S. L., Wilson B. C., Star W. M., van Gemert M. J. C. *Optical properties of intralipid: a phantom medium for light propagation studies* Lasers Surg Med 1992;12:510 - 519

[63] Wagnieres G., Cheng S., Zellweger M., Utke N., Braichotte D., Ballinni J., van den Bergh H. *An optical phantom with tissuelike properties in the visible for use in PDT and Fuorescence spectroscopy* Phys Med Biol 1997 ;42:1415 - 1426

[64] Bays R., Wagnieres G., Robert D., Theumann J. F., Vitkin A., Savary J. F., Monnier P., van den Bergh H. *Three-dimensional optical phantom and its application in photodynamic therapy* Lasers Surg Med 1997; 21:227 - 234

[65] Fullerton A., Stücker M., Wilhelm K. P., Wårdell K., Andersson C., Fisher T., Nilsson G. E., Serup J. *Guidelines for visualization of cutaneous blood flow by laser Doppler perfusion imaging.* Contact Dermatitis 46 I 3: 129-140, Blackwell (2002)

Appendix A

Epoxy phantom recipe

This epoxy phantom recipe is originally written by Johannes Swartling, and then modified by David Levitz. To fully understand how to make these phantoms the original document should be read.
Epoxy: Diglycidyl ether of bisphenol A (DGEBA) using an aliphatic amine hardener.
Chemical hazards! Make sure to follow the safety precausions valid for epoxy in preparing these phantoms.

A.1 Preparations

Figure out concentrations for each phantom Some useful tips/example: At 660 nm, μ_s' scales linearly as $7.75cm-1/$ (mg TiO2 / g epoxy). So, if $g = 0.75$ (from Appl Opt paper), μ_s (660 nm) scales by $3.1mm-1$ / (mg/g epoxy), and thus ţs $3.1 * M(TiO2)[mg]/122gepoxy$ or, at 660 nm, μ_s [mm-1] $0,0254 * M(TiO2)[mg]$.
A similar argument can be used to predict μ_s (and μ_a) at other wavelengths, if the coefficient slope per concentration is known.
For a quick calculation, use the Excel file *epoxy_recipe.xml*.
Note: You only use 43 g hardener per phantom; so adjust concentration appropriately.
Saturation: Hardener solutions tended to saturate when more than 400 mg TiO_2 per 43 ml hardener was used. Similarly, the absorbing toner stock solution saturates at concentrations greater than 120 mg / 100 ml.

Make cuvettes For each cuvette, you need 3 extra-large microscope slides (10 cm X 3 cm). Take the glass cutter and cut one of these slides into three pieces, about 3 cm long. Next, you make a sandwich: 1 whole slide + 2 of the pieces you just cut placed on the outside edges + another whole slide. Once you make (and align) the "sandwich", use 3 laundry clips to hold it together. Take an epoxy/hardener mix and glue all around the outside EXCEPT for a 3 cm opening, which you will later micropipette the phantom mix into. The glue should be applied with a match, and after applying it, the still wet "cuvette" should be held together using the 3 laundry-clips and dry for 24 hours.
Note: The epoxy/hardener glue mix you use is NOT the one to be used to make

the phantoms. There are 2 small containers from which the 2 components are squeezed out (they are quite pasty), and they should be mixed with a match. Tip: Make a handful of extra cuvettes. It is also recommended to calibrate your micro-pipette volume setting, so that you only need to empty it once to fill the entire cuvette. Practicing with water in an empty cuvette helps.

Oven Find oven and reserve it for the day you will need it. There is one oven at the ground floor of the machine shop in a room on the far left.

A.2 Procedure

For each phantom you need 2 polypropylene cups + epoxy + hardener + TiO2 + toner.
Hardener bottle and stock solution should only be opened in fume hood!
Always wear latex gloves when handling epoxy or hardener!

Make concentrated absorber stock solution and put in US bath Use 120 mg toner powder / 100 g liquid hardener. The measurements should be exact, and the solution should be kept in a capped flask. It is the flask that should be placed in the ultrasonic bath. A 250 ml solution should be stirred in the bath for about 2 hours.
Note: For the hardener, 1 ml 1 g
Note: Not capping the flask tightly will screw up the phantoms- if hardener mixes with air, it will foam about 10 minutes after mixing with epoxy.

For each phantom, make TiO2+absorber solution in hardener, put in US bath In this part, you will need to make a unique solution in a 170 ml pre-labeled polypropylene cup for each phantom. In each cup, mix:

- The proper amount of TiO_2,
- 43g hardener - mass of absorbing stock solution
- Absorbing stock solution

It's probably better to use a micropipette with the absorber stock solution. When the individual phantom solution is mixed, cap it and put it in the ultrasonic bath for some minutes (until solution looks homogeneous). If that doesn't work, shake the capped cup hard for a minute and see if dissolving increased; repeat if necessary.
Note:
Sometimes the cups with hardener solution float in the US bath. Adding some weight to keep them from floating is recommended.

For each phantom, add epoxy, stir until homogeneous When the cups come out of the ultrasonic bath, add the 122 g epoxy to the second pre-labeled phantom cup. Once the first cup done stirring, pour the hardener mix from the ultrasonic bath into the epoxy cup, and stir with a glass rod slowly until the solution is homogeneous. Stirring may take up to 45 minutes (or even more); you will not be done until the consistency is uniform throughout the phantom.

You may discard the first cup. A watch nearby may be useful but may also scare you (I recommend bringing a book or a second person to help or chat for this part). Phantom consistency is important; you don't want any air bubbles in there. Once you're done stirring, take the glass rod out, wait 1 minute, and stir again for another minute. Note: 1 full tablespoon of epoxy 25 g epoxy, and it's difficult to get exact measurements. Add the last few g of epoxy by letting them drip off a glass rod.

Put 1 ml sample in cuvettes Micropipette about 1 ml of each phantom into the cuvettes you prepared earlier. Be careful not to spill any phantom and make sure to avoid air bubbles; place the micropipette tip inside the cuvette during injection. Practice some a few times beforehand, it may be useful to slowly move the micropipette across the slab opening as you inject the mix into it. The cuvettes should be left standing right side up, and will NOT need to be baked in the oven. If you see air bubbles in there, try tapping them out with your finger. Any spilling of phantom onto the side of the microscope slides should be cleaned up- it will screw up integrating sphere measurements.

Wait 12-16 hours, put in oven for 24 hours After 12-16 hours, place phantoms on tray and take to oven in machine shop. Heat the samples at 55-60 C for 24 hours, remove, and machine if necessary.

Additional notes: At room temperature, some particles- either toner or TiO2 or microspheres- clump together, which will effectively change the scattering parameters. Also, some papers (i.e. Firbank et al 1993) claim TiO2 has large variations in particle size. More should be looked into that.

References:

- Original phantom recipe
- M Firbank and DT Delpy, emphA design for a stable and reproducible phantom for use in near infra-red imaging and spectroscopy, Phys Med Biol 38, p. 847-853, 1993.
- M Firbank, Motoki Oda, and DT Delpy, *An improved design for a stable and reproducible phantom for use in near infra-red imaging and spectroscopy*, Phys Med Biol 40, p. 955-961, 1995.
- J Swartling, JS Dam, and S Andersson-Engels, *Comparison of spatially and temporally resolved diffuse reflectance measurement systems for determination of biomedical optical properties*, Appl Opt 42, p. 4612-4620, 2003.

Appendix B

Matlab code

```
%%%%%%%%%%%%%%%%%%%%%%%%%%%%%%%%%%%%%%%%%%%%%%%
%Matlab file for simulations of DOCT measurements. This program creates
%images with the expected number of rings observed when measuring flows at
%a given velocity.
%%%%%%%%%%%%%%%%%%%%%%%%%%%%%%%%%%%%%%%%%%%%%%%

%Function generated in this program, DOCT(V_s). Input velocity, V_s, is
%the velocity of the moving scatterers in the sample.

function DOCT(V_s)

%Declaration of variables, and constants, needed for calculating the
%number of rings.
%Refractive index of the sample, i.e. blood and tissue:

n_t = ;

%Center wavelenght of the light source, 1300nm:

lambda_0 = 1300*10^-9;

%The Doppler angle, i.e. the angle between the incident beam and the moving
%scatterers. For this system theta = 69 degrees,i.e. (69 *pi)/180 radians.

theta = (69 * pi)/180;

%The A-scan aquisition rate. For this system f_scan=2000Hz.

f_scan = 2000;

%The delay equal to a period of A-scan.

tau_scan = 1 / f_scan;

%%%%%%%%%%%%%%%%%%%%%%%%%%%%%%%%%%%%%%%%%%%%%%%
```

```
%According to equation (4-2) in chapter 4 in the thesis the Doppler shift, f_s,
%is related to the velocity of the moving scatterers, V_s, as follows:
%f_s = (V_s * 2 * n_t * cos(theta)) / lambda_0
%%%%%%%%%%%%%%%%%%%%%%%%%%%%%%%%%%%%%%%%%%%%%%%%%%%%%%%%%%%%%%%%%%%%%%%%%%%%

%Calculating the Dopplershift f_s:

f_s = (V_s * 2 * n_t *cos(theta))/lambda_0;

%%%%%%%%%%%%%%%%%%%%%%%%%%%%%%%%%%%%%%%%%%%%%%%%%%%%%%%%%%%%%%%%%%%%%%%%%%%%
%According to chapter 4 in the thesis the monotonic range is given by +/-
%f_scan/4. When f_s > abs(f_scan/4) the auto correltion wraps around
%sinusoidally, creating rings with a period of f_scan.
%%%%%%%%%%%%%%%%%%%%%%%%%%%%%%%%%%%%%%%%%%%%%%%%%%%%%%%%%%%%%%%%%%%%%%%%%%%%

%%%%%%%%%%%%%%%%%%%%%%%%%%%%%%%%%%%%%%%%%%%%%%%%%%%%%%%%%%%%%%%%%%%%%%%%%%%%
%The value of the autocorrelation can, according to chapter 4 in the thesis, be
%witten as the expected value:
%R_(tau_scan)(f_s) = -sin(2 * pi * f_s * tau_scan - v_(n-1)) where
%v_(n-1) is a random phase noise term.
%%%%%%%%%%%%%%%%%%%%%%%%%%%%%%%%%%%%%%%%%%%%%%%%%%%%%%%%%%%%%%%%%%%%%%%%%%%%

%Calculating the number of rings, i.e. counts the number of times the
%R-function crosses the x-axis:

number_of_crossings = 0;

%Each ring is a period, i.e. two crossings:

number_of_rings = 0;

%Starting value for R, i.e. something to compare to:

R_old = 0;

%Checking that the absolute value of the Doppler shift, f_s, is larger than
%the absolute value of f_scan/4.

if abs(f_s) > abs( f_scan / 4 )

%Random phase noise term, v=v_(n-1). For v_(n-1)« 2*pi R is a sinusoidal
%function. Approximately:

v =0.1;

%Stepping from 1 to f_s with the step size 1 in order to build an image with
%rings:

for f = 1 : f_s
```

```
%Calculating the value of the autocorrelation function:

R = -sin(2 * pi * tau_scan * f - v);

%Since R is a descrete function it will never be zero, only close to it. In order
%to count the number of times the function becomes zero it checks when the
%old value and the new value of R %is on different sides of zero:

if ((R < 0 & R_old > 0) | (R_old < 0 & R > 0))

%Adds 1 each time a new crossing occurs:

number_of_crossings = number_of_crossings + 1;

%Calculates the number of rings:

number_of_rings = number_of_crossings/2;

end

R_old = R;

end

%%%%%%%%%%%%%%%%%%%%%%%%%%%%%%%%%%%%%%%%%%
%The value of number_of_rings gives the number of circles to be plotted in
%each image. The spacing between each circle is f_scan, and the scales on the
%x- and y-axis are given by f_s. In order to get the spacing right, the first
%circle is given the diameter d = f_s, and then the following circles get the
%diameters: d_n = f_s - n * f_scan (for circle number n).
%%%%%%%%%%%%%%%%%%%%%%%%%%%%%%%%%%%%%%%%%%

%Plotting the rings calculated above.

figure

%If number_of_rings is greater than zero, the rings will be plotted in the figure.

if number_of_rings > 0

%Stepping from 1 to number_of_rings with step size 1, in order to plot all
%of the rings.

for n = 1 : number_of_rings

%This command makes it possible to plot all the rings in the same figure.

hold on;

%Gives the figure a title.
```

```
title('DOCT image with rings due to high velocities')

%Gives the diameter, d, of each ring:

d = f_s - n * f_scan;

%Alpha is the angle needed to plot a circle, and goes from -pi to pi with step
%size 0.001.

alpha = -pi : 0.001: pi;

%Radius of the circle with diameter d:

r = d / 2;

%Plots a circle with radius: r = d / 2:

plot(r * sin(alpha), r * cos(alpha))

end

hold off;

end

else

%If the absolute value of f_s is smaller than the absolute value of f_scan there
%will be no rings to draw. Hence printing "No rings should be observable"

fprintf('No rings should be observable');

end

%Printing how many rings there should be in the figure:

fprintf('There should be %g rings in the figure.',number_of_rings)
```